The Design and Construction of a Second Harmonic Generation Microscope For Collagen Imaging

A thesis submitted in partial fulfillment

of the requirements

for the Degree of Master of Science in Medical Physics (Clinical)

Ivy Win Long Au

The University of Canterbury

2012

Table of Contents

List of Figures

Acknowledgements

First and foremost, I would like to thank my project co-supervisor Dr Frédérique Vanholsbeeck for offering me this interesting and enjoyable project, and without whom, this project would not have been possible. I really appreciate her support, encouragement and ideas throughout the course of this project.

I would also like to thank my other supervisor Dr Jon-Paul Wells for sourcing the equipment for the microscope and for his support throughout the year.

To the Biophotonics team at the University of Auckland, thank you Isha for measuring the thickness of the tissue samples for me, Norman for his trouble-shooting skills and Dr Stephane Coen for his expertise in optics.

I would like to express my appreciation to Dr Cather Simpson, Peter Hosking and Dr Stuart Murdock for the use of their PMT's. Also, thanks to Dr Adrian Turner for lending me the microscope lenses, and Satya Arimapu and Jennifer Sweny for providing me with tissue samples.

Finally, I would like to thank Antoine Runge and Dr Claude Aquergaray for the use of their laser. Their time and energy spent on the maintenance the laser is most appreciated.

Abstract

In recent years, second harmonic generation (SHG) microscopy has revolutionised the field of biological imaging by offering a new means of visualising the fine structures of collagen tissues with excellent image penetration while minimising photodamage.

This project involves the design and construction of a SHG microscope that is built around a compact femtosecond fibre laser for collagen imaging. Operating at 1032 nm, the microscope has demonstrated a penetration depth of beyond 320 microns in collagen, which is considerably superior to depths of 250 to 300 microns achievable with a conventional SHG microscope coupled to a Ti:sapphire excitation laser.

The imaging characteristics of the microscope have been tested with a modified sample of bovine pericardium. The results indicate the microscope is polarisation-sensitive to the tissue structure and is capable to detecting signal changes at 10 μm resolution.

This thesis will describe in detail, to our best knowledge, the first SHG microscope equipped with a compact and robust all-fibre femtosecond 1032 nm laser source.

Chapter 1. Introduction

1.1 Objectives

There are three principal objectives to this project, firstly, to design and build a versatile second harmonic generation (SHG) microscope to be coupled to a compact, custom-built 1032 nm all-fibre excitation laser for structural imaging of collagen tissues. The project also involves the optimisation of the microscope and a quantitative study on the effects of changing the optical parameters of the imaging setup. The third objective is to extract structural information from collagen samples and to evaluate the imaging properties of the microscope.

1.2 Introduction to Second Harmonic Generation (SHG)

Second harmonic generation is one of the many phenomena within the branch of physics known as nonlinear optics. Under normal conditions a medium exhibits a linear response to light, where it is assumed that optical properties such as the refractive index, absorption coefficient and reflectivity are independent of the optical power. However, this approximation is only valid at low power levels. With the advent of lasers in 1960 and the rapid development of mode-locked lasers since the early 1980's, optical powers escalated to a level where the response of the medium started to deviate from the linear behaviour [1]. At sufficiently high light intensities the optical response of the medium was found to be dependent on the light intensity. The discovery of the nonlinear interactions of light with matter opened up an entirely new field of nonlinear optics, allowing various intriguing phenomena such as second harmonic generation and other frequency mixing processes to be investigated.

Figure 1-1. Schematic diagram of a second-harmonic wave of frequency 2ω generated by an excitation wave of frequency ω in a nonlinear optical medium.

As illustrated in Figure 1-1, SHG is the nonlinear process where part of the energy of an optical wave of frequency ω propagating through a nonlinear medium is converted to a wave of 2ω, at twice the original frequency. SHG is also known as frequency-doubling, which is a special case of sum frequency generation. It is a parametric process, characterised by the relationship $\omega_1+\omega_2=\omega_3$. In the case of SHG, The frequency of the pump is $\omega_1=\omega_2$ and the output harmonic frequency, ω_3, is twice the frequency of the pump.

One of the fundamental applications of SHG is the generation of new frequencies from a laser with a fixed wavelength and to extend the frequency range of available laser sources. As the theories and techniques of nonlinear optics became increasingly complicated, SHG has found a greater range of applications ranging from providing a means of verifying some fundamental aspects of quantum theory to the study of optical surfaces [2,3]. Another important application of SHG is the emerging field of SHG microscopy. In particular, there has been rapid development within the last decade on new techniques for studying and visualising the fine structure of collagen tissues.

SHG microscopy has several advantageous features that make it an ideal imaging modality for studying biological samples and living organisms. As SHG is a parametric process which arises from an induced polarisation rather than from absorption, damage to the sample by photobleaching and phototoxicity is significantly reduced compared to other modes of nonlinear microscopy. In addition, the relatively long near-infrared wavelengths typically used in SHG microscopy offer excellent depths of penetration and are well tolerated by intact tissue samples. Furthermore, the polarisation-sensitivity of the SHG process can be exploited in SHG microscopy for determining the absolute orientation of protein molecules and their degree of organisation in the tissue sample [4].

1.2 Thesis Outline

In Chapter 2, the theory behind second harmonic generation (SHG) and some of the important properties of SHG in relation to SHG microscopy will be addressed. Special emphasis will be given to the origin of second-harmonic waves and the conditions required for efficient SHG.

Chapter 3 will examine the numerous factors that need to be considered in the construction of a basic SHG microscope. Factors such as the choice of a suitable laser and aspects of the design of the microscope will be discussed in detail.

Based on the basic knowledge of the design of a SHG microscope discussed in the previous chapter, Chapter 4 will describe the design of the actual microscope and its ancillary devices used in this project to perform biological SHG imaging.

In Chapter 5, the experimental results obtained with the SHG microscopy will be presented and discussed.

Finally, an improved SHG microscope design is implemented and described in Chapter 6.

Chapter 2. The Theory of SHG- Second Harmonic Generation

This chapter will present a theoretical treatment of SHG from a classical point of view. Light interaction with matter will be considered as the response of a dielectric medium at the atomic level to the electric fields of an intense light beam, or simply, as a polarisation induced by the incident beam.

In Section 2.1, an overview of the theory of nonlinear optics will be covered and a brief mathematical description of harmonic generation will be explored. Section 2.2 will focus on the origin of the second-order nonlinear phenomenon, second harmonic generation. The intensity-dependence and the criticality of phase-matching in SHG will then be discussed. As an example of the application of phase-matching, the method of angle-tuning a BBO crystal as a means of phase-matching is presented in Section 2.4.

In the SHG process, not all the frequency-doubled light will travel in the forward direction (in the same direction as the propagating excitation laser). Section 2.5 will discuss the emission directionality of SHG signals.

Since the excitation laser does not simply propagate as a plane wave but as a focused beam with a certain beam waist, Section 2.6 will examine SHG of a Gaussian beam.

SHG is used widely in SHG microscopy for imaging the fine structures of collagen tissues. In Section 2.7, the suitability of collagen as a sample for SHG and the type of information extractable from the SHG images will be discussed.

2.1. Theory of Nonlinear Optics

The linear relationship between the polarisation and electric field is strictly true in linear optics, where the susceptibility is not a function of the electric field. In nonlinear optics we need to consider the consequence of a changing electric susceptibility, and all its subsequent optical properties, as it varies with the strength of the electric field of the incident light beam [1,5].

In this section, a few approximations were made what regards to the light source and the media. The excitation laser is assumed to be a monochromatic, non-magnetic and linearly polarised beam with no free charge satisfying the slowly varying envelope approximation.

The optical properties of a medium are expressed by the real and imaginary parts of the dielectric constant, ε_r, which is derived from the polarisation $\vec{P}$ of the medium:

$$\vec{D} = \varepsilon_0 \vec{E} + \vec{P} = \varepsilon_0 \varepsilon_r \vec{E} \tag{2.1}$$

The origin of second harmonic signals can be explained by examining the response of an atomic system to an applied electric field. At lower excitation intensities where the optical response of a medium is linear, the relationship between the induced dielectric polarisation $\vec{P}$ and the electric field $\bar{E}$ of the incident radiation is linear and is given by:

$$\vec{P} = \varepsilon_0 \chi^{(1)} \vec{E} \tag{2.2}$$

where $\chi^{(1)}$ is commonly known as the linear susceptibility [6].

Equation (2.2) served as a good approximation for many years because the electric field strengths technologically achievable in those early years were much weaker than the fields inside atoms and molecules. It was not until the 1870s that the refractive indices of specific solids and liquids were demonstrated to be altered by the application of a strong field by Rev. John Kerr [1]. This, observation, characterised by a change in refractive index proportional to the square of the applied DC field, was the first nonlinear optical effect to be demonstrated. This phenomenon is now known as the DC Kerr effect [1,5].

The combination of Equations (2.1) and (2.2) gives the relationship between ε_r and χ:

$$\varepsilon_r = 1 + \chi^{(1)} \tag{2.3}$$

In nonlinear optics, the relationship between $\vec{P}$ and $\vec{E}$ could be generalised as the summation of a first order response $P^{(1)}$ and a series of nonlinear terms of increasing order:

$$\vec{P} = \vec{P}^{L} + \vec{P}^{NL} = \vec{P}^{(1)} + \vec{P}^{(2)} + \vec{P}^{(3)} + \cdots \quad (2.4)$$

where $\vec{P}^{(n)}$ is the n^{th} order nonlinear polarisation [1,6].

By combining Equations 2.2 and 2.4, the nonlinear response of the material can be expressed as a Taylor expansion in terms of the applied electric field $\bar{E}$:

$$P = \varepsilon_0(\chi^{(1)}E_\omega + \chi^{(2)}E_\omega E_\omega + \chi^{(3)}E_\omega E_\omega E_\omega + \cdots) \quad (2.5)$$

Here, the coefficients $\chi^{(n)}$ correspond to the tensor of the n^{th}-order nonlinear process.

The linear susceptibility$\chi^{(1)}$ is much greater than the nonlinear susceptibilities and hence optical nonlinearities are only noticeable at high-amplitude fields. This means that the material response to incident fields of weak to moderate intensities will be linear to a very good approximation. With larger fields, the higher-order terms in the Taylor expansion become significant as the response of the electrons inside the medium becomes nonlinear. With extremely large fields ($E_{incident} \geq E_{atom}$) the Taylor expansion breaks down and the electrons are ripped from the atoms by optical field ionisation [7].

2.2 The Theory of Second Harmonic Generation

SHG is a nonlinear optical process where a laser beam of frequency ω is frequency-converted to generate a new optical field at frequency 2ω. Historically, SHG was the most important nonlinear interaction as it was the first nonlinear optical phenomenon to be discovered and has a much stronger intensity than the higher-order harmonics [8].

Consider a monochromatic beam of amplitude E_0 and angular frequency ω, expressed as

$$E = E_0 \sin \omega t. \quad (2.6)$$

When this electric field is incident on a nonlinear material, the resulting electric polarisation is

$$P = \varepsilon_0\chi E_0 \sin \omega t + \varepsilon_0\chi^{(2)}E_0^2 sin^2\omega t + \varepsilon_0\chi^{(3)}E_0^3 sin^3\omega t + \cdots \quad (2.7)$$

Using basic trigonometry, the polarisation can be rewritten as

$$P = \varepsilon_0 \chi E_0 \, sin\, \omega t \; + \frac{1}{2}\varepsilon_0 \chi^{(2)} E_0^2 \, (1 - cos\, 2\omega t) + \frac{1}{4}\varepsilon_0 \chi^{(3)} E_0^3 \, (3 sin\, \omega t - sin\, 3\omega t) + \cdots \tag{2.8}$$

The second harmonic term of the polarisation is therefore:

$$P^{(2)} = \frac{1}{2}\varepsilon_0 \chi^{(2)} E_0^2 \, (1 - cos\, 2\omega t) \tag{2.9}$$

Equation (2.9) shows two points of interest in the second harmonic term. The first term suggests that the second-order polarisation consists of a component at zero frequency, known as optical rectification [8]. As this term does not lead to the generation of electromagnetic radiation, this DC electrical field will be ignored in this discussion.

The second term, $cos\, 2\omega t$, corresponds to changes in the electric polarisation at twice the fundamental frequency, generating light that radiates at frequency of 2ω. This process is commonly known as second-harmonic generation, or SHG [7].

An important aspect of the Taylor expansion in Equations (2.7) and (2.8) is that all even-order coefficients must disappear for media with inversion symmetry. As most materials possess inversion symmetry, SHG is only observed in a limited range of nonlinear crystals and some specific biological tissues with inversion asymmetry [8].

2.3 Nonlinear Materials

Optical materials are divided into two main categories based on whether their structures remain unchanged upon space inversion.

From Equation (2.5), the quadratic term implies that a medium responds differently according to the direction of the electric field. For a mathematical explanation, consider $P_x = \varepsilon_0 \chi^{(n)} E_x^n$ in one dimension. Under inversion symmetry, P_x must change sign if E_x changes sign. However, when n is even, E_x^n remains unchanged if $E_x = -E_x$. Consequently, in materials that have inversion symmetry, $\chi^{(2)}$ is zero and these media cannot undergo second harmonic generation [1].

Second-order nonlinear optical interactions can only occur in non-centrosymmetric materials, i.e. materials that do not display inversion symmetry. A large nonlinear coefficient is a necessity, although not a sufficient condition for efficient second harmonic generation.

2.3.1 Intensity

SHG occurs as a result of part of a medium's atomic response that depends quadratically on the strength of the applied optical field. Consequently, the intensity of the SH light $I_{2\omega}$ tends to increase as the square of the intensity of the applied laser light I_{ω} as given by:

$$I_{2\omega} = \frac{1}{2} I_{\omega}^2 \sqrt{\frac{\mu_0}{\varepsilon_0}} \frac{L^2}{n_{\omega}^2 n_{2\omega}} \left(\frac{\omega \chi^{(2)}/c}{\Delta kL/2} \right)^2 sin^2 \left(\frac{\Delta kL}{2} \right). \quad (2.10)$$

where μ_0 is magnetic constant, ε_0 is the electric constant, L is the length of the nonlinear medium, n_{ω} and $n_{2\omega}$ are the refractive indices experienced by the fundamental and the second harmonic waves, respectively, in the nonlinear medium, Δk is the change in wave number and c is the speed of light [6].

The first nonlinear optics experiment of the laser era was performed by Peter Franken at the University of Michigan in 1961 [1,9]. By focussing a ruby laser into a 1-mm slab of quartz crystal, Franken and his team were the first to experimentally observe a detectable second harmonic signal. However, the harmonic intensity was so weak that the photographic plate reproduced in the 15 August 1961 issue of Physical Review Letters appeared totally blank [9]. In fact, the energy conversion efficiency from fundamental to harmonic was about one part in a hundred million (10^8), a clear demonstration that SHG was a real effect but it was too minuscule to be put into any practical use. Within a few months of Franken's experiment, researchers at Ford Motor Company had exploited the property of birefringence and phase-matching of KDP crystals to significantly increase the conversion efficiency [1]. To understand the reason behind the low efficiency, one needs to appreciate the importance of phase-matching in SHG.

2.3.2 Phase-Matching

The magnitudes of nonlinear optical processes are generally small and they tend to decrease with higher orders of harmonic. This implies that a nonlinear medium of sufficient length is

required to obtain useful nonlinear conversion efficiency. To achieve maximum SHG conversion efficiency, the phase of the second harmonic waves generated throughout the crystal must be the same to allow the coherent summation of the fields. This condition is called phase-matching [1,5,6,7].

To appreciate the importance of phase-matching, we begin by examining Franken's experiment in 1961, where a very weak 347.15 nm-SHG signal was generated by focussing a ruby laser (694.3 nm) into a quartz crystal. Assuming that the field of the ruby laser is a plane wave propagating in the z-direction, written as:

$$E_1 = A_1 \cos[\omega t - k_1 z] \tag{2.11}$$

where k_1 is the angular wave number of the fundamental beam with $k_1 = \frac{n_1 \omega}{c}$, and n_1 is the refractive index experienced by the fundamental wave in the crystal [1,6].

The polarisation component of the second-harmonic term is thus:

$$P^{(2)} = \frac{1}{2}\varepsilon_0 \chi^{(2)} A_1^2 \cos[2\omega t - 2k_1 z] \tag{2.12}$$

which appears logical at first. However, a comparison of the space-time dependence in Equation (2.11) with that of a freely propagating field at twice the same frequency is simply:

$$E_2 = A_2 \cos[2\omega t - k_2 z] \tag{2.13}$$

where $k_2 = \frac{n_2 \omega}{c}$ by analogy with k_1. Note that the arguments of the cosines in Equations (2.11) and (2.12) are different unless $2k_1 = k_2$ ($\Delta k = 0$), which is only true if $n_1 = n_2$. However, as all materials are dispersive, the refractive index of the quartz crystal is different at 694.3 nm and 347.15 nm [1,6].

Consequently, the second harmonic and the fundamental waves will propagate with a different phase velocities and the second-harmonic waves generated at the front will arrive at the back of the quartz crystal at a different time to the fundamental as shown in Figure 2-1 (b). Thus the 347.1 nm waves generated at the back of the crystal will be out of phase with those generated at the front.

To quantify the severity of the phase-mismatch, the distance over which the cosine terms in Equations (2.11) and (2.12) are π radian out of phase is commonly known as the coherence length:

$$l_c = \frac{\pi}{|k_2 - k_1|} = \frac{\lambda}{4|n_2 - n_1|} \tag{2.14}$$

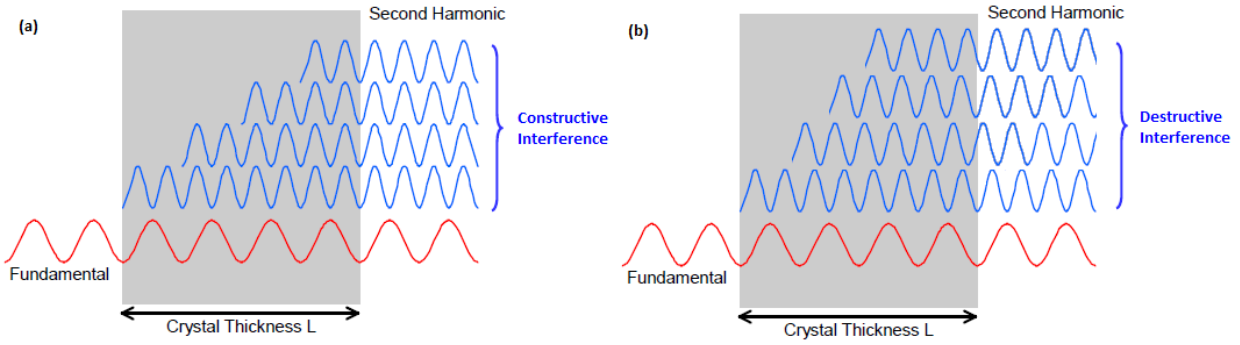

Figure 2-1. (a) A schematic of the concept of phase-matching were all the induced dipoles radiate in-phase in the forward direction so that all contributions add up constructively, (b) phase-matching is not satisfied and the second harmonic contributions interfere destructively. Modified from [11].

A typical value for the coherence length is in the order of tens of microns, meaning only a few microns of the 1-mm quartz crystal was contributing to the extremely weak SHG signal observed [1].

As mentioned in the last section, the phase-matching problem was shortly solved by exploiting the birefringence in a KDP crystal to keep the fundamental and second-harmonic waves constantly in-phase with each other. By careful adjustment of the crystal orientation so that the reflective index of the ordinary wave at ω was the same as the one for the extraordinary wave at 2ω, a SHG conversion efficiency of over 10% was observed [1,9].

The phase-matching of the radiated electric field is critical in the observation of SHG signals. Phase-matching ensures that the second harmonic contributions from all positions in the crystal add up coherently and do not get cancelled out by destructive interference [11]. The condition of phase-matching in a nonlinear crystal is illustrated in Figure 2-1 (a). This condition is commonly satisfied by making use of the birefringence in anisotropic crystals. In particular, the SHG property of the BBO crystal will be described in detail in the next section.

2.4 SHG in the BBO Crystal

Beta barium borate (β-Ba_2BO_4), also commonly known as BBO crystal, is one of the most important nonlinear optical crystals used in laser optics due to its excellent optical properties such as a wide spectral range for nonlinear frequency conversion that extends from the UV to infrared [12,13]. It possesses a wide optical transmittance range of 190-3500 nm and a high laser damage threshold. BBO is also a chemically stable crystal with a high melting point of 1095°C and a wide range of temperature stability [14].

The salient feature of the BBO crystal is anisotropy and its angle-tuning range for phase-matching. BBO is an uniaxial birefringent crystal. At 1032 nm, it has a refractive index of 1.6558 for the ordinary-ray (n_0) and 1.5429 for the extraordinary-ray (n_e) at room temperature [13]. BBO has a remarkably high effective nonlinear coefficient (d_{eff}= 1.94 pm/V), which is approximately four times higher than another common nonlinear crystal, potassium titanyl phosphate ($KTiOPO_4$), or KDP crystals. This means BBO has a much higher efficiency in second harmonic generation than KDP [12,14].

In birefringent nonlinear crystals, the refractive index of the ordinary (o-ray) is different to that of the extraordinary ray (e-ray) at a given wavelength. In theory, phase-matching can simply be achieved by an appropriate choice of laser polarisation and direction of propagation to force the fundamental wave to propagate as an o-ray and the SHG as the e-ray [6]. Therefore, with clever arrangement, the BBO crystal can be manipulated to obtain $n_1 = n_2$, or $\Delta k = 0$ to generate high intensities of SHG.

BBO is a negative uniaxial crystal and its SHG process can be described as the combination of two ordinary waves at ω to generate an extraordinary wave at 2ω, which can be further described by the shorthand $o + o = e$ [6].

To find the phase-matching angle θ_m , one needs to examine the index of an ellipsoidal surface

$$\frac{x^2}{n_o^2} + \frac{y^2}{n_o^2} + \frac{z^2}{n_e^2} \tag{2.15}$$

Figure 2-2 represents the index ellipsoid of the BBO crystal at the x=O plane [8]. By simple trigonometry:

$$|OA| = n_e(\theta),$$

$$y = |OA| \cos\theta = n_e^2(\theta) sin(\theta),$$

$$z = |OA| \sin\theta = n_e^2(\theta) cos(\theta).$$

$$\frac{n_e^2(\theta) cos^2\theta}{n_o^2} + \frac{n_e^2(\theta) sin^2\theta}{n_e^2} = 1 \tag{2.16}$$

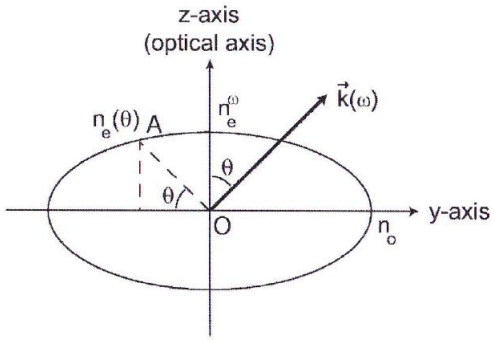

Figure 2-2. Index ellipsoidal surface of BBO, where $n_e^{2\omega} < n_o^{\omega}$, at the x=O plane [8].

The refractive index of the extraordinary ray varies with its propagation direction θ to the optical axis according to:

$$\frac{1}{n_e^2(\theta)} = \frac{cos^2\theta}{n_o^2} + \frac{sin^2\theta}{n_e^2} \tag{2.17}$$

where n_o and n_e are the refractive indices for the o- and e- waves, respectively.

For a negative uniaxial crystal where $n_e^{2\omega} < n_o^{\omega}$, there exists a phase-matching angle θ_m at which

$$n_e^{2\omega}(\theta_m) = n_o^{\omega}. \tag{2.18}$$

where $n_e^{2\omega}(\theta_m)$ is the refractive index of the e-ray at the second-harmonic frequency at the phase-matching angle, and n_o^{ω} is the refractive index of the o-ray at the fundamental frequency. This means that if the fundamental beam is generated along the same direction as the o-ray, the SHG beam will be generated along the same direction as the e-ray. This situation is illustrated in Figure 2-2.

By combining Equations (2.16) and (2.17),

$$\frac{1}{(n_o^{\omega})^2} = \frac{1}{\left[n_e^{2\omega}(\theta_m)\right]^2} = \frac{sin^2\theta_m}{(n_o^{\omega})^2} + \frac{cos^2\theta_m}{(n_e^{\omega})^2} \tag{2.19}$$

Finally, solving for θ_m:

$$sin^2\theta_m = \frac{(n_o^{2\omega})^{-2} - (n_o^{2\omega})^{-2}}{(n_e^{2\omega})^{-2} - (n_o^{2\omega})^{-2}} \tag{2.20}$$

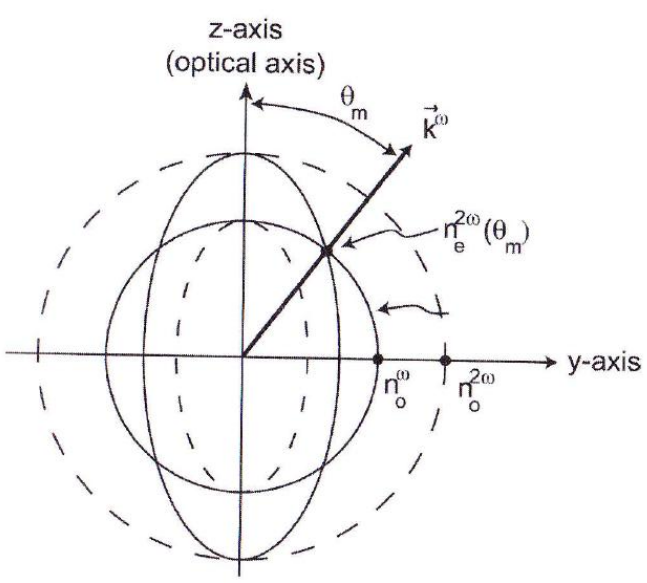

Figure 2-3. Normal surfaces for both e- and o-rays in the BBO crystal. Phase-matching occurs at $\boldsymbol{\theta_m}$, when $\boldsymbol{n_e^{2\omega}(\theta_m) = n_o^{\omega}}$ [8].

When the excitation is propagating along this phase-matching angle, the frequency-doubling process will have a phase-mismatch of $\Delta k = 0$. This implies that, theoretically, the coherence length l_c will approach infinity when this condition is met.

Figure 2-3 uses the normal (index) surface to show the refractive index of the e- and o-rays as a function of frequency for illustrating the phase-matching condition of a negative uniaxial crystal, such as the BBO crystal [8]l. In normal dispersion, the refractive index of the 2ω-wave is higher than the one of the ω-wave. Thus, the index surface at 2ω is larger than the one at ω. For a negative uniaxial crystal ($n_e^{2\omega} < n_o^{\omega}$), the e-ray surface is within the o-ray surface. Therefore,

when the fundamental wave propagates as an e-ray and the second harmonic wave as an o-ray, their normal (index) surfaces will intersect at the phase-matching angle θ_m [8,16].

The above argument is an oversimplification of phase-matching in the BBO crystal and it must be stressed that under arbitrary conditions, Equation (2.19) may not necessarily possess a solution for a physically meaningful orientation angle θ. In cases where the sample's dispersion in the linear refraction index is too large or when the birefringence is too small, the right-hand side of the equation can be larger than unity, resulting in no solution [6]. However, it should be clear from Equation (2.16) that phase-matching could be achieved by rotating the crystal with respect to the crystal axis at particular orientations or by altering the polarisation of the laser beam. A quantitative study on phase-matching of the BBO crystal is described in detail in Chapter 5.

2.5 Emission Directionality of SHG

SHG is a quasi-coherent process characterised by a specific emission pattern comprising a forward and a backward SHG component with respect to the direction of the excitation beam. In SHG imaging, the SHG creation ratio (F_{SHG}/B_{SHG}) is a quantitative measure of the emitted forward- and backward-propagating SHG signal. Although there remains some controversy on the interpretation of the SHG creation ratio, several studies have established that the directionality of the SHG signal is a direct measure of the degree of structural organisation in the tissue [15]. Specifically, regular structures with sizes comparable to the excitation wavelength will predominantly emit a forward-propagating SHG signal, resulting in a large F_{SHG}/B_{SHG} ratio. Conversely, emissions from smaller and more irregular structures will produce a less forward-directed signal, denoted by a smaller SHG creation ratio, although $F_{SHG}/B_{SHG} \geq 1$.

2.6 SHG of Focussed Gaussian Beams

In the discussion so far, the excitation wave has been approximated as an infinite plane wave. However, in reality, it is usually focussed into the nonlinear optical medium as a focussed Gaussian beam to take advantage of the quadratic relationship between the excitation intensity and the resultant SHG intensity. From Equation (2.10), it is easy to see that the focussing of the beam into a tiny spot can dramatically increase the strength of the SHG output.

Propagating as a focussed Gaussian beam, the excitation beam acquires an additional phase-shift that differs from that for a plane wave of the same frequency [1]. This phase difference is called the Gouy phase-shift:

$$\varphi_{Gouy}(z) = -\tan^{-1}\left(\frac{z}{z_R}\right) \tag{2.21}$$

where z_R is the Rayleigh length and z_R=0 corresponds to the position of the beam waist.

If a beam is focussed into an infinite length of nonlinear crystal exhibiting normal dispersion (Δk >0), no net SHG signal will be generated. In practical terms, this means that negligible SHG signal is produced when the focal point lies within the medium and many Rayleigh lengths from either the front or the back surface of the crystal [17]. This is explained by the effect of the Gouy phase-shift on the normal dispersion that results in the cancellation of the harmonic contributions from sources upstream and downstream of the focus by destructive interference.

A good way to circumvent this problem is to limit the extent of the nonlinear crystal within the focal region so that the cancellation of the SHG contributions to the two sides of the focus is no longer complete. With a thicker nonlinear crystal, the focus can be moved near the front or back surface, or even positioned outside the crystal altogether [17].

In Chapter 5, several sets of SHG experiments are performed by examining the SHG intensity as a function of depth in a crystal near the front crystal surface.

2.7 SHG in Collagen Tissue

Collagen tissue is used extensively in second harmonic microscopy due to its abundance in biological materials and its unique structural properties [18]. Making up approximately 30% of the whole-body protein content, collagen samples are readily available from most connective tissues, such as skin and tendon, and internal organs [19,20]. Thus, the majority of studies on SHG microscopy have been performed on collagen-rich tissues [18].

Single non-centrosymmetric molecules will generate a frequency-doubled signal via SHG, but the signal intensity will be much stronger if the molecules are arranged in a crystalline array. Hence, biological tissues that possess both a crystalline structure and non-centrosymmetry are often good candidates for SHG imaging [21].

Collagen is highly crystalline and has a structure of a triple-helix consisting of three α-chains hydrogen-bonded together. The individual molecules are arranged into fibrils of 20 to 250 nm in diameter, which assemble into fibres with diameters of between 500 nm to 3 μm [19]. SHG microscopy has demonstrated itself to be an exquisitely sensitive imaging modality for studying collagen at high resolution, with diffraction-limited resolution (sub-300 nm) easily achievable [22].

Recently studies have reported significant differences in the SHG signals recorded between normal and experimental-damaged collagen sample, which means that pathological changes can potentially be detected [22,23]. Furthermore, SHG microscopy has demonstrated its ability to detect structure changes in breast, ovarian and skin cancers, opening up a new avenue for a potentially useful imaging tool in oncology [24,25,26].

2.8 Summary

This chapter has explained that nonlinear optical processes such as SHG only arise from the incidence of an intense beam of light onto certain optical media. At excitation intensities below the threshold for nonlinear optical interactions, the response of the media will be largely linear.

In SHG, the structure of the optical medium is crucial and the process is limited to samples with an inversion asymmetric structure. SHG is heavily dependent on the excitation intensity and the degree of phase-matching in the sample. The emission of SHG in a sample has a certain directionality depending on the level of organisation in its structure. The SHG creation ratio, F_{SHG}/B_{SHG} is used to quantify the degree of organisation.

SHG is useful in high-resolution microscopy and it has successfully demonstrated the ability to discriminate diseased tissues from healthy ones in a wide range of cancers.

Chapter 3. SHG Microscopy

SHG microscopy has been used extensively in studying the structures of well-ordered protein assemblies, such as collagen, microtubules and muscle myosin [22]. In the past decade, SHG microscopy has been progressively established as a nondestructive imaging modality that holds promise for both basic research and clinical pathology.

This chapter will introduce and discuss various aspects of the instrumentation involved in SHG microscopy. In particular, considerations of the excitation laser in terms of the excitation wavelengths and laser powers will be examined in Section 3.1.1. The effects of the common features of microscope objectives, such as their values of numerical aperture and working distance will be discussed in Section 3.1.2.

Finally, a comparison of the imaging abilities of SHG will be made with two other types of nonlinear optical microscopy, namely, two-photon excitation fluorescence (TPEF) microscopy and third harmonic generation (THG) microscopy.

3.1 A Microscope for SHG Imaging

The basic requirements for an SHG microscope is a scanning microscope coupled to an excitation laser. However, in order to extract useful information from a sample, a number of modifications must be considered and implemented. The most basic design of a SHG microscope capable of forward and backward SHG imaging is shown in Figure 3-1.

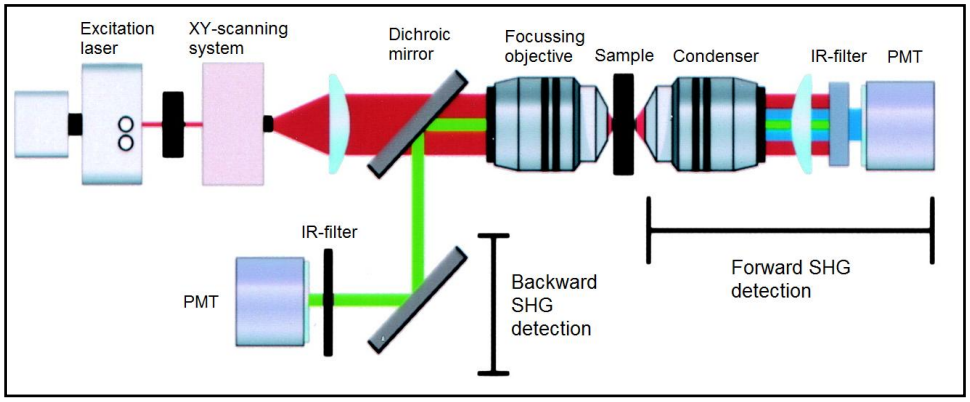

Figure 3-1. Layout of a basic second harmonic microscope [27]

SHG microscopy works by raster-scanning the excitation beam across the sample to scan the focal point along the x- and y-axes. The laser then passes through the objective to focus the beam on the sample to generate frequency-doubled light. In transmission mode, the forward-propagating light gets collected by the condenser while in reflection mode, the backward light is collected by the objective to be detected by a photomultiplier (PMT) tube [27]. The resulting electronic signal is generally recorded and analysed by imaging software.

3.1.1 Laser Source

3.1.1.1 Considerations on Excitation Wavelength

The most common laser source for SHG microscopy is the titanium: sapphire (Ti:S) laser operating at approximately 800 nm [28]. In general, the production of second-harmonic signals is not a resonant process so the choice of excitation wavelengths is not critical to the intensity of the SHG. However, the measured SHG intensities in thick biological samples are highly dependent on the excitation wavelength due to processes such as scattering and absorption inside the sample [29]. At shorter wavelengths, the excitation beam is more susceptible to

multiple scattering and absorption events, resulting in low tissue penetration. Conversely, longer excitation wavelengths will yield greater penetration depths and also achieve superior tissue viability [28,29].

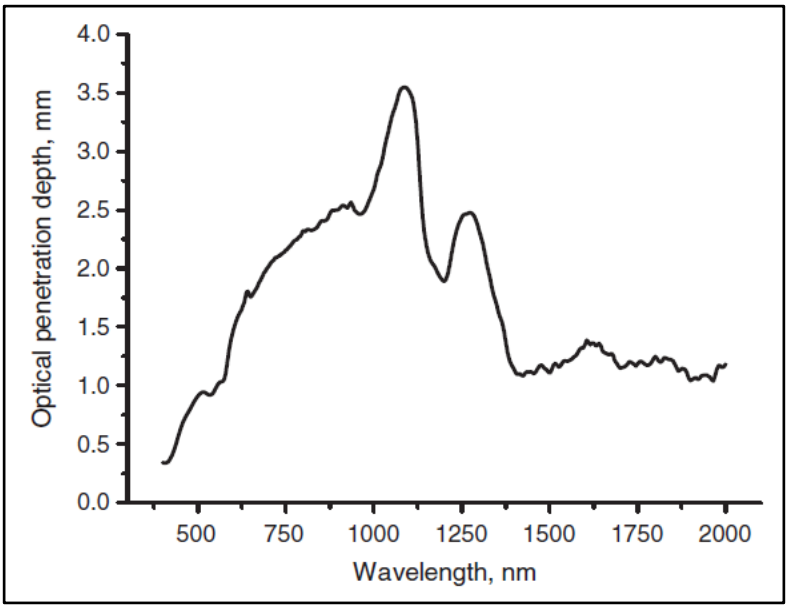

Figure 3-2. Penetration depth of light of different wavelengths in human skin [30].

A past study on the optical properties of human skin found that, after tissue absorption and scattering have been accounted for, the maximal penetration depth of light is 3.5 mm observed at 1090 nm as plotted in Figure 3-2 [30]. Water absorption significantly reduces the biological transparency at wavelengths of above 1300 nm, thus the use of longer excitation wavelengths for increasing image penetration is not a feasible solution [31].

3.1.1.2 Considerations on the Excitation Laser Power

The first scanning SHG microscope was implemented in 1978 by Gannaway and Sheppard for microscopic studies of inorganic SHG crystals. However, the range of specimens that could be imaged was limited by their use of a 1060 nm continuous wave (CW) laser [32]. The detection of SHG signal with sufficient sensitivities could only be possible with high input laser powers that would be intolerable to biological specimens. Hence, there was limited development in biological

SHG microscopy until the advent of pulsed lasers in the 1980s that finally provided the required power densities to exploit the characteristics of nonlinear optical phenomena [18,20].

As the intensity of second-harmonic light is dependent on the square of the input flux density, maximisation of the SHG process will require creating ultra-short pulses of minimal duration. Techniques such as Q-switching and mode-locking allow the generation of pulses of extremely high instantaneous powers in conjunction with low total power averaged over time [18]. Past studies have verified that femtosecond laser pulses are more effective in generating second harmonic signals than picosecond or nanosecond pulses, with no compromise on tissue damage [21].

3.1.2 Microscope Objectives

As with most modes of biological imaging, a compromise in the spatial resolution, penetration depth and efficiency must be made to optimise the imaging ability of the imaging device. The ideal SHG microscope is equipped with objectives with long working distances (WD), medium numerical apertures (NA) and optimised for transmission of the excitation near-infrared laser [32]. In addition, the objective must also be transparent to the second harmonic signal when working in the reflection configuration.

Typically, a water-immersion objective with 0.8-NA is used for its long working distance (1-3 mm) which is ideal for deep tissue imaging [32]. While an objective with higher-NA would theoretically produce a smaller focal volume and thus achieve a high resolution, these objectives typically have insufficient working distances of less than 200 µm. In addition, a study in 1979 had found that at above 1.0-NA, the excitation laser polarisation would be altered by high-NA induced polarisation aberrations [17,32].

At below 0.50-NA, the great reduction in peak power and the resulting drop in SHG intensity together with a low resolution would render the objective unsuitable for SHG microscopy. Thus, the ideal objective should have an NA of 0.50 to 0.90 and WD of 1 to 3 mm [17].

When operating in transmission mode a microscope condenser must be added on the other side of the sample to collect the SHG light. A condenser with a higher NA than the excitation objective is preferred so that it can collect as much signal as possible, since the SHG phenomenon is localised with the focal volume [32].

3.2 Comparison with other Modes of NLO Microscopy

In this section, a holistic comparison of the salient features of SHG microscopy will be made with two other nonlinear optical microscopy modalities, namely, two-photon excitation fluorescence (TPEF) microscopy and third harmonic generation (THG) microscopy.

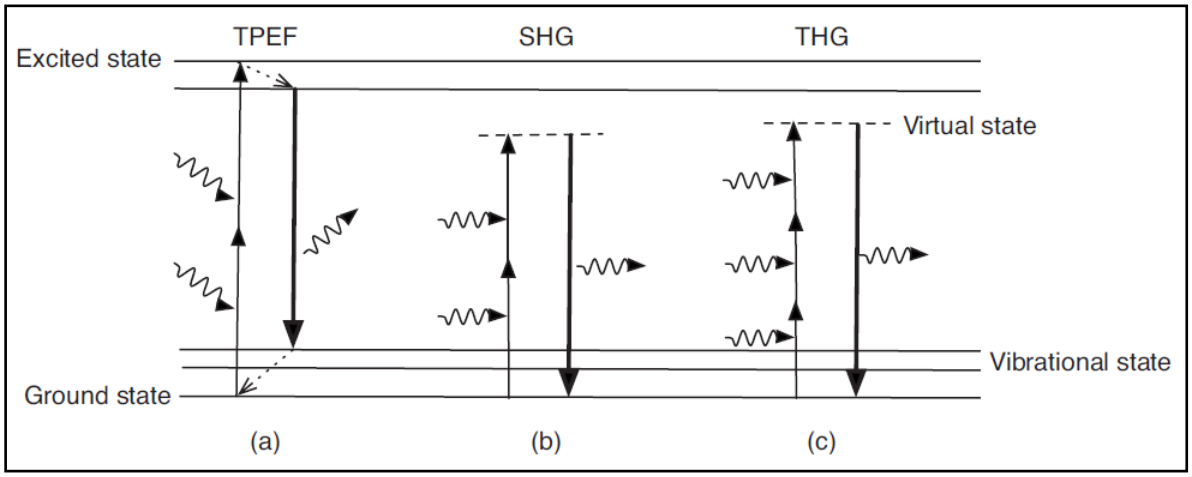

Figure 3-3. Energy level diagrams comparing the nonlinear process: (a)TPEF, (b) SHG, and (c) THG. Wiggley lines represent incoming and radiated photons and dashed arrows non-radiative relaxation processes [33].

Two-photon excitation fluorescence (TPEF) microscopy

TPEF microscopy is the most frequently-used nonlinear optical imaging modality and is currently firmly established as a useful tool in biological imaging [33]. However, with a fluorescence-based contrast mechanism, photodamage to the sample is inevitable in TPEF microscopy [34]. As illustrated in Figure 3-3 (a), TPEF is a nonparametric process involving the absorption of two photons and excitation of the fluorophore molecule in the sample to an excited state, which is then remitted as a fluorescent photon after some non-radiative decay [33]. As TPEF involves the absorption of energy by the specimen, a major drawback of TPEF microscopy is photobleaching [34].

Second harmonic generation (SHG) microscopy

SHG is a fast-emerging nonlinear technique that by-passes the issue of photodamage. As a parametric process characterised by an unchanged initial and final quantum-mechanic state, the marked advantage of SHG microscopy is the lack of energy deposition in the specimen [33]. A

quantum mechanical description of SHG is shown in Figure 3-3 (b), where two fundamental photons are annihilated to form a new photon at double the frequency.

SHG is a powerful imaging technique that can acquire biological images with high contrast, high spatial resolution, optical 3D sectioning and a good penetration depth with minimal tissue invasion. Perhaps the largest limitation of SHG microscopy is its limited applicability to a small number of biological structures due to its requirement of the non-centrosymmetry in the sample [34].

Third harmonic generation (THG) microscopy

THG is a similar process to SHG that involves the annihilation of three photons to form a frequency-tripled photon. In third-order processes such as THG, the third-order susceptibility $\chi^{(3)}$ is non-zero in centrosymmetric materials [6], so in theory, THG microscopy can be used to image an ordinary block of glass and other liquids and gases that lack symmetry-breaking. However, the intensity of THG is much weaker than SHG signals and its imaging practicality is restricted to regions with sudden changes in refractive index, such as tissue surfaces or interfaces between tissue layers [34].

Summary of Nonlinear Optical Microscopy

Given that the signal intensity of SHG and TPEF is proportional to the square of the light intensity, and THG, to the cube of the light intensity, this means only the tissue within the focal volume of the focused excitation beam is efficiently generating a nonlinear signal [34]. An important advantage of nonlinear optical microscopy is its inherent optical-section ability to acquire sharp, two-dimensional tomographic images by eliminating all signal contributions out of the focal plane of the sample.

In recent years, there has been increasing interest in multicontrast nonlinear microscopy, which is a microscope designed for the simultaneous detection of the TPEF, SHG and THG signals. Multicontrast nonlinear microscopy allows different contrast mechanisms of the three nonlinear processes to acquire parallel images of the same sample, which enables different functional structures in the sample to be examined [33,35].

3.3 Summary

This chapter has highlighted the important considerations for the design of a SHG microscope. The ideal excitation source is a mode-locked laser generating laser pulses of the order of femtoseconds with an excitation wavelength of between 800 and 1100 nm for optimal tissue penetration. The ideal focusing microscope should have a numerical aperture (NA) of 0.5 to 0.9 and a long working distance of over 1 mm. If operating in the reflection mode, the condenser needs a higher NA than the focusing microscope for effective SHG signal collection.

In comparison to other modes of nonlinear microscopy of collagen tissues, SHG pose a far lower risk of photodamage to the sample than TPEF microscopy. It is also more suitable for imaging bulk tissue samples than THG microscopy.

Chapter 4. Preliminary Design of SHG Microscope

Although commercial systems for second-harmonic imaging are currently available, there are several advantages in building a custom-built setup. An important advantage is the flexibility in selecting all the components of the imaging system, including the microscope, scanning unit and the laser source. This allows for careful tailoring of each component of the system to the particular requirements of SHG microscopy. Another consideration is price. Commercial systems are generally quite expensive while a custom-built one can be made at a fraction of the price. But the ultimate advantage of a customised system is the understanding of its complete operations. An intimate understanding of the system is required for effective trouble-shooting when a problem arises, for example, when the laser beam needs realigning or an optical component needs replacing.

This chapter will describe in detail each component of the SHG microscope and the rationale behind how they are fitting to the design. With the 1032 nm excitation laser being the ‘heart’ of the SHG microscope, the construction of the microscope is largely tailored to the features of the laser and all components are optimised to operate at approximately 1032 nm.

4.1 Experimental Setup

Initially, one of the main goals of the project was to build the SHG microscope by simply coupling an infrared laser to an existing scanning microscope. However, the microscope was later found to be unavailable so the goal was switched to the design and construction of a SHG microscope by putting together individual optical components. Figure 4-1 is a photograph of the experimental setup used for all SHG measurements throughout the project.

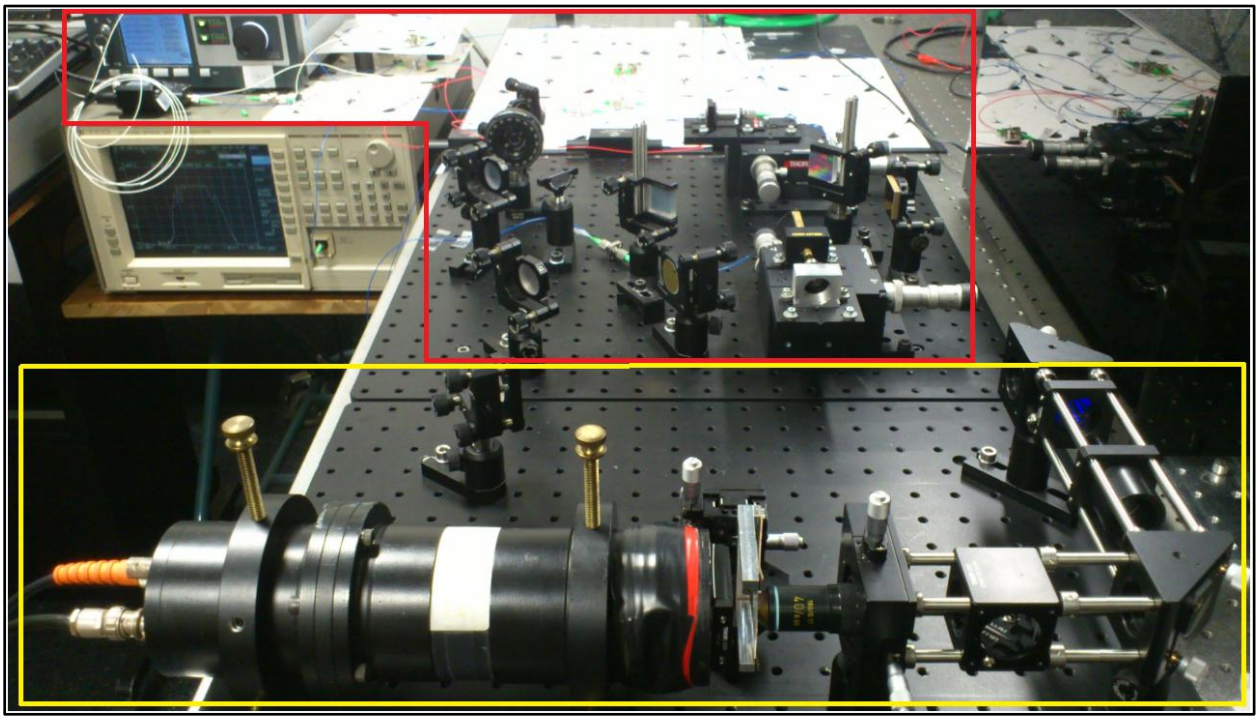

Figure 4-1. Photograph of the experimental setup used in the project.

All components within the boundaries of the red line make up the excitation laser source while the main body of the SHG microscope is contained within the yellow boundary. The important features of the laser, the microscope, and the diagnostic devices used in this project will be discussed in full detail in the following sections.

4.1.1 Laser and Laser Diagnostics

The laser used in this project is a unique device built and developed over the years by members of the Department of Physics at the University of Auckland. This mode-locked Yb-doped fibre laser is used as an excitation light source and coupled to an optical compressor to generate

linearly polarised 325 fs pluses at a wavelength of 1032 nm with an amplified average power of 89.7 mW and a repetition rate of 5 MHz. A detailed description of the laser design and its performance has previously been published [36,37].

To generate pulses in the range of femtoseconds, the laser output from an all-fibre laser must undergo optical compression before reaching the microscope. Figure 4-2 shows a schematic diagram of the layout of the laser source coupled to the compressor, which consists of all the optical components between the laser output and the SHG microscope.

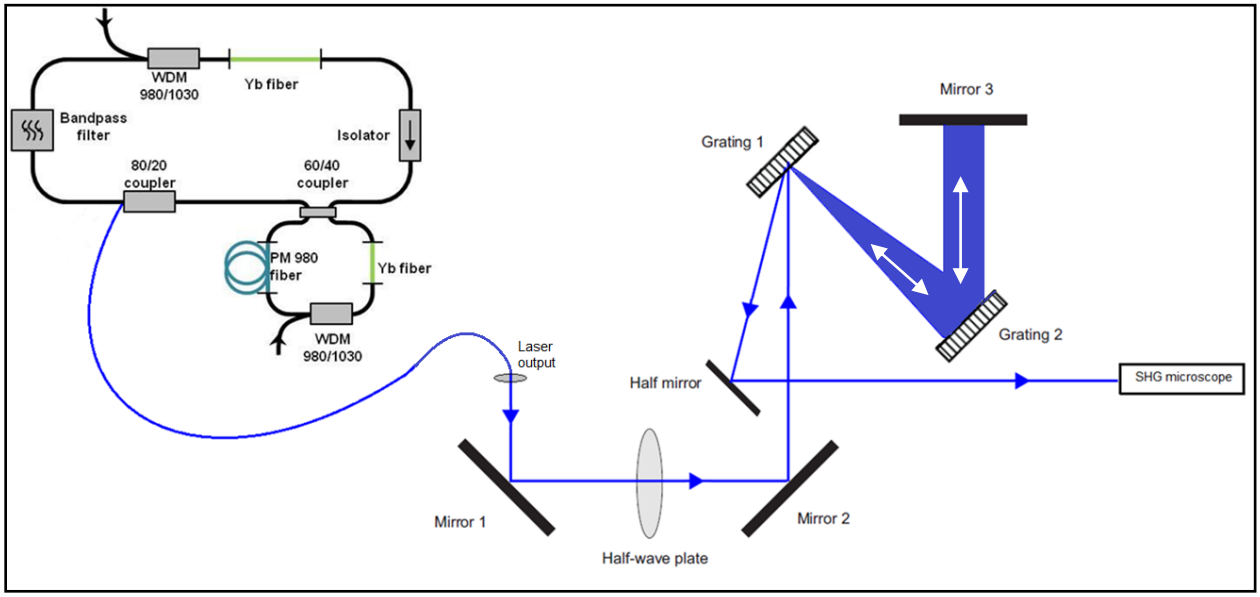

Figure 4-2. Diagram of the fibre laser coupled to the pulse compressor (size not to scale). The smaller diagram on the top-left-hand corner shows the main components of the laser and right half of the figure shows the optical layout of the compressor.

To ensure that the laser is fit for SHG throughout the duration of entire sets of experiments, it is essential that part of the laser beam is diverted to diagnostic equipment. A spectral analyser is the most crucial device for real-time beam monitoring, providing quantitative measurements of the pulse length and the spread of the wavelengths present in the beam. It is also a useful indicator of whether the laser has remained mode-locked during an experiment. Under mode-locking, the spectrum analyser would produce an output spectrum similar to the one in Figure 4-3 with a broad spectrum centred at 1032 nm. If mode-locking ceases, the spectrum will collapse to a narrow peak. An Ando AQ-6315A optical spectrum analyser is used to monitor the laser beam during experiments at all times.

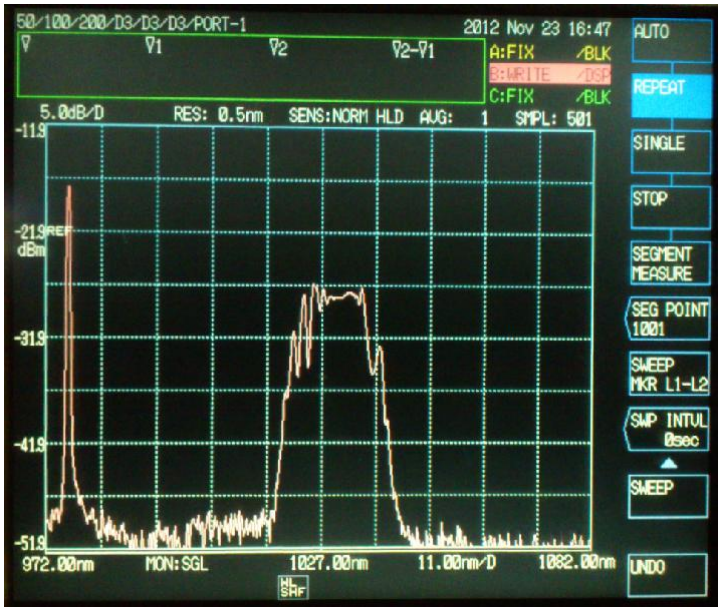

Figure 4-3. Output spectrum of the excitation laser.

A power meter is another essential diagnostic tool. A Melles Griot broadband power/energy meter (13PEM001) is used throughout the experiments to measure the laser power all along the beam path and to aid in beam alignment to minimise power loss in the microscope. The power meter also has the important role of detecting abnormalities in the incident excitation laser. A drop in power is often a useful warning that the laser is either out of alignment, failing to mode-lock, or the internal optics are requiring cleaning.

A digital real-time oscilloscope (Tektronix TDS 220) is used to monitor the train of pulses generated by the pulsed laser. It acts as a monitor to make sure that the laser is running in single-pulse mode and generating regular distinct individual pulses at 5.263 MHz (as seen in Figure 4-4 with some unwanted detector ringing). If the laser pulses are generated in train-mode, they are observed as an irregular series or train of pulses generated at frequencies above 5 MHz. As the energy contained in each pulse is inversely related to the pulse repetition rate (pulse energy = $\frac{Power}{f_{rep}}$), under train-mode, the laser will no longer be delivering the peak power required for optimal SHG. An irregular display of pulse pattern is an indication that the laser current needs adjusting to keep the laser in single-pulse mode.

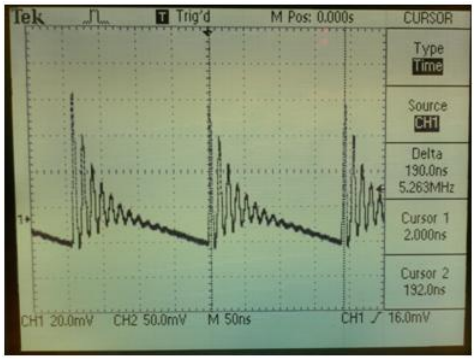

Figure 4-4. Oscilloscope displaying the pulse-trains generated by the pulsed laser.

A Spiricon (SP503U) silicon CCD camera is used to examine the profile of the laser beam and to measure the beam diameter so that the peak intensity incident on the sample could be calculated.

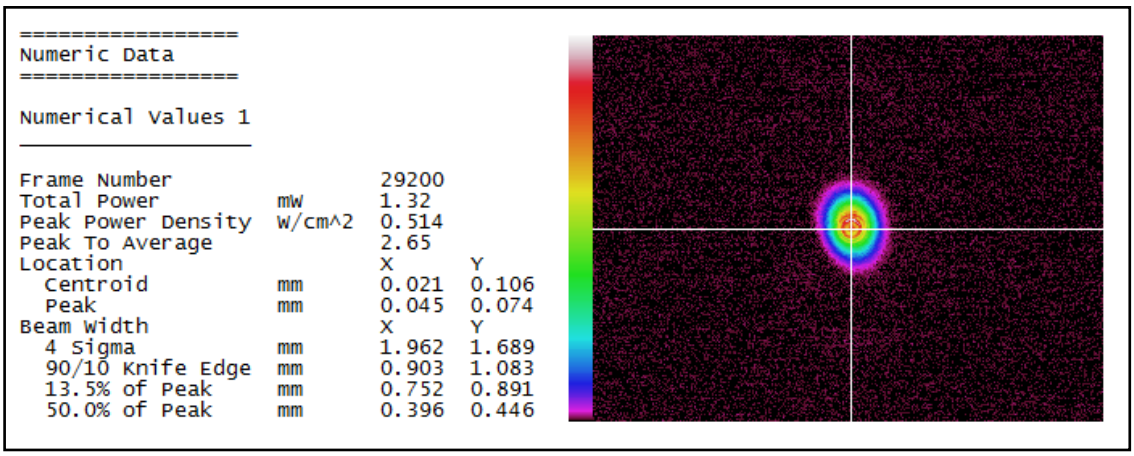

```
==================
Numeric Data
==================

Numerical Values 1
__________________

Frame Number                 29200
Total Power          mW      1.32
Peak Power Density   W/cm^2  0.514
Peak To Average              2.65
Location                     X       Y
  Centroid           mm      0.021   0.106
  Peak               mm      0.045   0.074
Beam Width                   X       Y
  4 Sigma            mm      1.962   1.689
  90/10 Knife Edge   mm      0.903   1.083
  13.5% of Peak      mm      0.752   0.891
  50.0% of Peak      mm      0.396   0.446
```

Figure 4-5. Beam profile of the excitation laser beam

Figure 4-5 clearly shows that the profile of the beam resembles a Gaussian beam. The image was taken at normal incidence to the beam just before the back aperture of the excitation objective. Although a measurement of the peak power is made, this value does not reflect the true peak value because a -20 dB (1%) and a -30 dB (0.1%) filter have been fitted to avoid damaging the CCD detector. The true value is calculated using the assumptions made in Gaussian optics where $2\omega_0 = \frac{4\lambda}{\pi}\left(\frac{f}{d}\right)$. With an average intensity of 17.6 mW measured by the power meter just before the objective and a calculated beam area of 1.69×10^{-4} cm^2 at the focus,

the peak laser intensity on the sample is calculated to be 61.2 MW/cm^2, which is well below the 100 MW/cm^2 damage threshold of biological tissues [28].

4.1.2 The Microscope

Beam alignment is critical for minimising signal losses in SHG microscopy so most optical components that form the main body of the microscope are housed in cage mounts for enhanced stability and accurate optical alignment. All components within the boundary of the dashed lines in Figure 4-6 are mounted on cage mounts to make the imaging system more robust and less susceptible to misalignment.

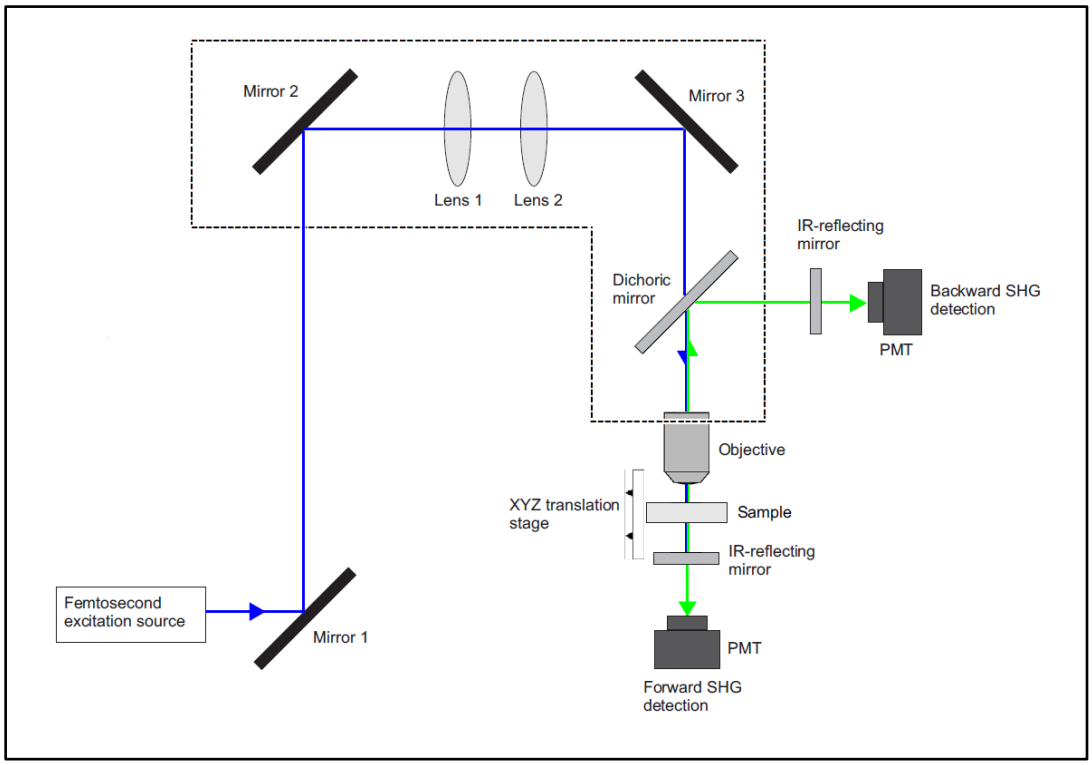

Figure 4-6. Optical layout of the SHG microscope, the blue lines show the beam path of the excitation laser and the green lines show that of the SHG signal.

Immediately downstream of the laser output, the beam is precisely aligned by Mirrors 1 and 2 to propagate through the centre of Lens 1 and 2. Owing to the long optical path between the laser and the sample (approximately 2 m), beam divergence becomes an issue. Therefore, the laser beam needs to be collimated, and its spot size reduced, to avoid being clipped by the objective entrance. The two lenses are strategically positioned to form a telescope system to reduce the

beam size and to correct for the divergence of the laser so that maximal incident light is collected by the microscope objective. A third mirror is used to ensure perfect alignment of the laser beam to the objective lens. From the mirror, the beam then passes through a long-pass dichroic mirror to be focussed by the microscope objective onto the sample. The objective is held in an XY-translation mount to make sure that the laser light is incident at the centre of its back aperture. For 2D data acquisition, the laser beam needs to scan across the surface of the sample. As there was insufficient equipment for constructing a scanning system at the time the experiments were performed, three translation stages were stacked and mounted on a tilt stage to allow movement of the sample in all three directions with respect to the stationary incident beam.

Upon incidence of the excitation beam, the sample will emit frequency-doubled light (516 nm) in both the forward and backward directions. For forward SHG measurements, the microscope will operate in transmission mode where the forward component of the SHG light will keep propagating in the same direction along with the laser beam. The 1032 nm laser light will then be filtered out by the IR-reflecting mirror so that only the SHG signal will be detected by the PMT. The backward SHG signal will be recollected in reflection mode by the microscope objective and be reflected at 90° off a dichroic mirror to be detected by the PMT. The long-pass dichroic mirror together with the IR-reflecting mirror will ensure the elimination of any residual fundamental light before reaching the PMT. As only one PMT is available at any one time, simultaneous SHG signal detection in the backward and forward directions is unachievable.

Microscope Objectives

In order to increase the conversion efficiency of SHG, the SHG microscope requires a microscope objective to focus the laser beam onto a specific spot in the sample. A number of objective lenses with different numerical apertures (NA) are tested:

Nominal Magnification	Manufacturer/ Type	N.A.	Working Distance (mm)
25×	Melles Griot/04 OAS 014	0.50	1.30
40×	Melles Griot/04 OAS 012	0.65	0.47
80×	Nikon/LU Plan	0.80	1.00
100×	Nikon/LU Plan	0.90	1.00

Table 4-1. Specifications of the microscope objectives used in the experiment.

4.1.3 SHG Detector

Two different photomultiplier (PMT) modules are used in the course of this project. For the earlier experiments, a Thorlabs PMT (Thorlabs, PMM01) is employed while an EMI 6255B PMT is used in the latter half of the project.

The spectral response of the Thorlabs PMT is shown in Figure 4-7. With a functional window between 280 nm and 630 nm, the PMT is an ideal detector for the SHG microscope as it is sensitive to the 516 nm SHG signal while remaining unresponsive to the 1032 nm excitation laser. In comparison to the other PMT, this Thorlabs PMT is a lot more compact and is much more user friendly. With a built-in high voltage circuitry, it eliminates the need for an external power supply typically required for operating conventional PMT modules. It is powered by a standard 12 V power supply and its gain is controlled by adjusting a home-made variable 0-1.25 VDC power supply. All SHG signals presented in the first half of Section 5.1 and the entire Section 5.2 are acquired using the Thorlabs PMT.

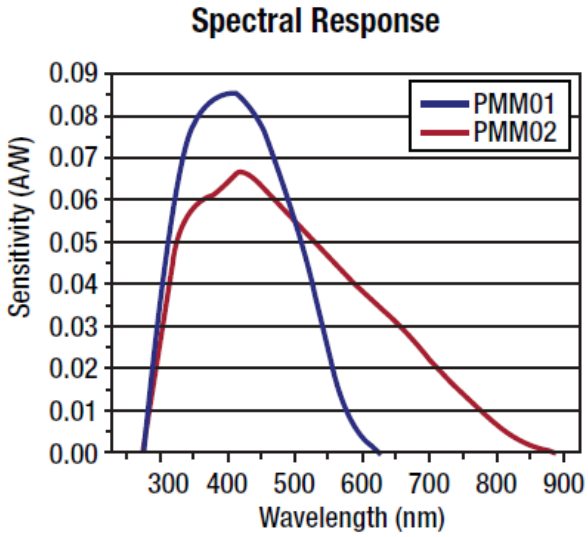

Figure 4-7. Spectral response of the PMM01 PMT (please refer to the blue curve), [38].

For all other experiments, a much older EMI PMT is used for signal acquisition. Unfortunately, little is known or can found on the behaviour of this PMT because no user's manual or any specification documents could be found.

An external high voltage power supply is required to operate the EMI PMT. In this project, a Brandenburg (Model 2478R) photomultiplier power supply is used and the PMT gain is varied by changing the current to the PMT. By trial-and-error, a current of 1250 V is found to be optimal for acquiring SHG with a decent signal-to-noise ratio without damage to the PMT.

Another Tektronix TDS 220 oscilloscope is used to display the SHG signal output from the PMT. Each individual measurement is taken by manually lining up the marker on the y-axis with the SHG signal and reading off the value at the bottom-right corner of the screen. Originally, a fully digital data acquisition system was planned and successfully implemented for real-time data acquisition and display. A data acquisition (DAQ) module (National Instruments USB-6215B) was coupled between the PMT and the computer to display the instantaneous response of the PMT using the LABVIEW software. However, the light emitted from the computer screen was noticeably disturbing the SHG signal even with its brightness adjusted to the minimum setting and with a black curtain placed over and around the entire microscope. Consequently, all SHG measurements are made by manually recording the value of the SHG intensity displayed on the oscilloscope.

During SHG signal acquisition, every attempt is made to prevent any unwanted background light from reaching the PMT to increase the signal-to-noise ratio. Originally, a black box was constructed to fit perfectly over the entire microscope to keep out all room light. However, the box was no longer suitable when the Thorlabs PMT (160 cm^3) was replaced by the substantially larger EMI PMT (924 cm^3). Subsequently, all measurements made with the EMI PMT are acquired with the microscope fully covered with a matt black curtain in a room in complete darkness.

All free-space optical components of the laser and the microscope are rigidly secured to an optical table with active vibration isolation.

Chapter 5. Results and Analysis

A number of quantitative experiments are made using the SHG microscope to study the SHG signal response to changes in the excitation light. Sections 5.1 and 5.2 investigate the effects of different excitation intensities and phase-matching conditions on the SHG signals originating from a BBO crystal.

Different microscope objectives are then tested with the microscope to optimise it for biological imaging in Section 5.3. Measurements of both the forward- and backward-propagating SHG are made to ensure that the microscope is capable of working in the transmission, as well as the reflection mode.

The first biological studies are made in Sections 5.4 and 5.5 with a sample of modified bovine pericardium. The polarisation-dependence of SHG microscopy is demonstrated using the tissue sample, and finally, a ‘depth-scan’ of the tissue is perform in the two imaging modes to extract structural data from the bovine sample.

As the responses of the PMTs are not calibrated to their corresponding intensities in units of W m^{-2}, all SHG measurements in this section are expressed in terms of arbitrary units (a.u.).

5.1 Dependence of the SHG Intensity on the Power of the Excitation Laser

A major challenge of SHG detection, particularly in transmission mode, is the separation of the frequency-doubled signal from the co-propagating laser light, which will typically be several orders of magnitude greater than the intensity of the SHG signal [18]. Although an infrared-blocking filter has been placed at the detector entrance of the PMT, it may still be insufficient for the complete elimination of the fundamental light. Hence, experiments must be carried out to ensure that the fundamental excitation light does not contribute to the signal detected by the PMT. In Section 2.3.1, it has been established that the efficiency of the SHG process is dependent on the square of the laser intensity. To verify whether the signals detected by the PMT were indeed generated via the SH process, PMT readings were recorded while focussing the laser beam at different average laser powers of 1.38 mW to 17.9 mW inside a BBO crystal. The laser power was varied by altering the current to the pump laser and it was measured with a power meter at the exit of the microscope objective. To obtain the laser power measurements, the power meter was used in place of the PMT. Figure 5.1 shows the relationship between the PMT response and the square of the incident laser power. Note that for all experiments in this section, a -20 dB neutral density (ND) filter is added to the detector head of the PMT to reduce the incoming signal by 99%.Due to the high frequency conversion efficiency of BBO crystals, the SHG signals produced by higher excitation intensities can easily saturate the PMT detector. Therefore, an ND filter is added to avoid damage to the PMT.

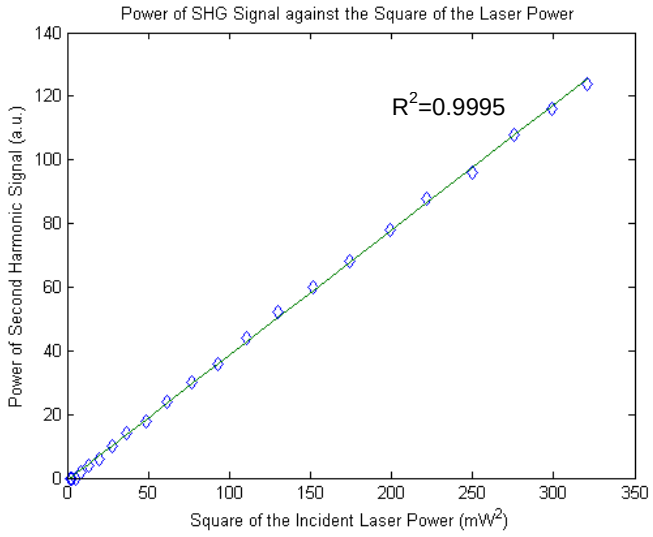

Figure 5-1. Linear dependence of SHG intensity on the square of the excitation power as demonstrated by the Thorlabs PMT.

Figure 5-1 shows that the measured SH intensity is quadratically proportional to the excitation power. With a coefficient of determination (R^2) between 0.90 and 1.0, statistically there is a very strong linear relationship between the square of the laser power and the SHG intensity. This finding is a confirmation that the detected signal is indeed generated from SHG.

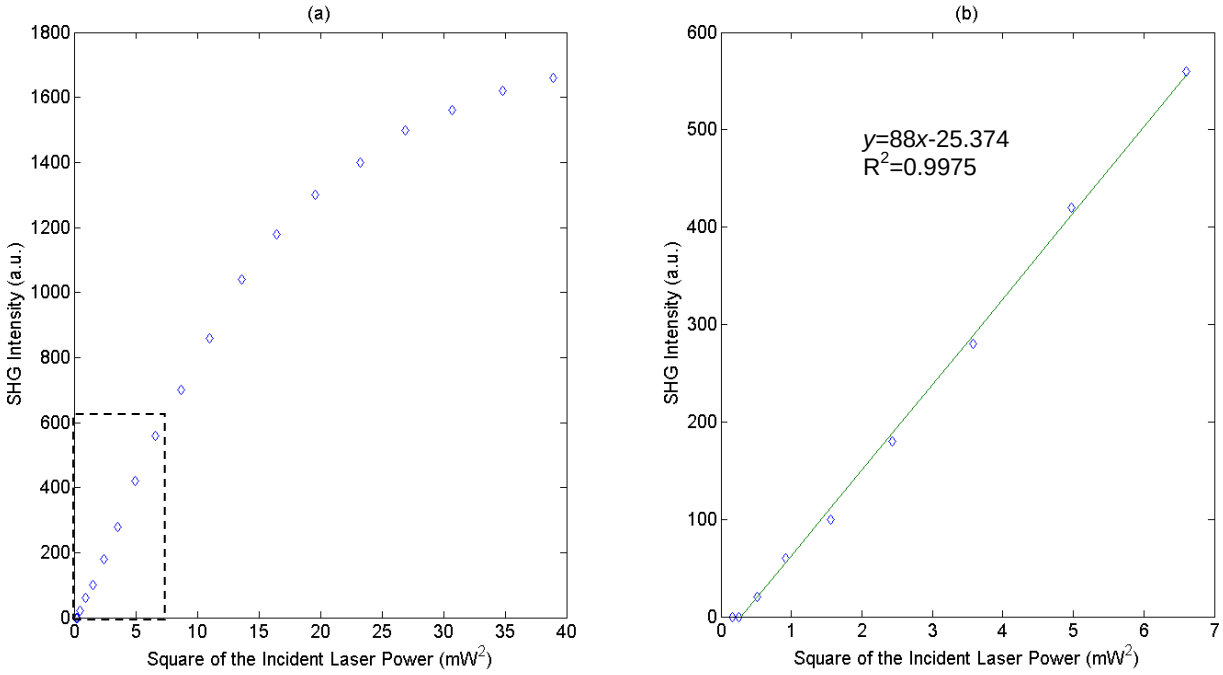

Figure 5-2. (a) SHG intensities recorded against the square of the laser power, (b) enlarged plot of the linear region in the EMI PMT's response.

The Thorlabs PMT was no longer available in the second half of this project and it was replaced by the EMI PMT. The same experiment is repeated to test the response of the PMT and the results are plotted in Figure 5-2 (a). The linear region inside the dashed box is enlarged and shown in Figure 5-2 (b).

From the figure, we observe that the EMI PMT has a much narrower operational window but a much higher sensitivity than the original Thorlabs PMT. The figure also shows that unlike the original PMT, this new PMT does not have a linear response to light of different intensities. At above average excitation power of 15 mW^2, its sensitivity tends to decrease with increasing incident laser power, which is an indication of signal saturation, while at lower incident laser powers the PMT exhibited a linear response. As the intensities of the SHG signals associated with biological microscopy are typically several orders of magnitude lower than that of the

excitation laser beam, this PMT was considered suitable for SHG imaging despite its lower limited operational range. Subsequently, all measurements acquired in the latter half of the project were performed using the EMI PMT. It must be noted that all SHG signal intensities above 560 arbitrary units (a.u.) are potentially underestimated due to the nonlinear response of the PMT. Thus, all SHG measurements over 560 a.u. will be corrected for the nonlinearity in the following sections.

5.2 Phase-Matching in BBO Crystals

As BBO is an anisotropic crystal, angle tuning of the crystal will allow the phase-matching conditions to change through changing the refractive indices inside the crystal. In this exercise, the BBO crystal is securely mounted at the centre of a rotational mount. The laser beam is then carefully collimated to propagate through the centre of the crystal. Extra care is taken to ensure that no part of the beam is incident on the outer edges of the crystal. Because the SHG process is sensitive to the symmetry-breaking resulting from an interface between two media, beam-incidence on the edge of the crystal will produce a sizeable jump in the SHG intensity. Figure 5-3 shows the SHG signal recorded at each angle as the BBO crystal is manually rotated at angular intervals of 3 degrees over 180 degrees in transmission mode.

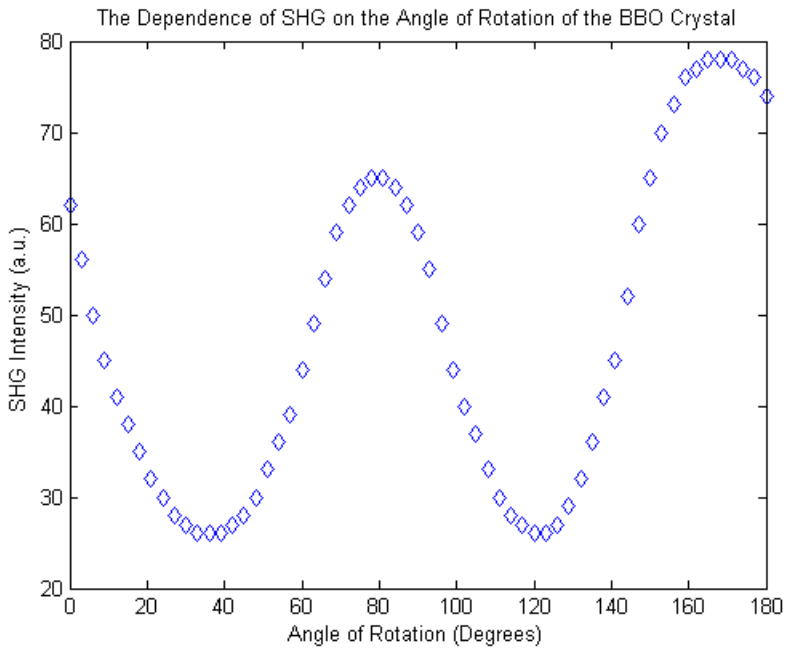

Figure 5-3. SHG signal as a function of the BBO crystal's angle of rotation.

The BBO crystal, apart from its SHG capability, is also birefringent because of its anisotropy and possession of an axis of symmetry, often referred to the optical axis. This means that when light refracts in the BBO crystal, it is split into two beams: a) the ordinary ray which obeys Snell's law and b) the extraordinary ray that does not. The two rays are linearly polarised orthogonally to each other with the ordinary beam polarised orthogonally to the optical axis, resulting in the two rays having differing phase-velocities and refractive indices. Whereas n_o is constant, n_e is dependent on the direction of beam propagation due to its dependence on the direction of polarisation with respect to the optical axis. Thus, when the BBO crystal is rotated about the axis of the incident beam, the ordinary ray would remain fixed while the extraordinary ray would precess about the axis of rotation.

Furthermore, the value of $n_e(\theta)$ varies between a maximum, n_o, which occurs when the extraordinary ray propagates parallel to the optical axis, and a minimum, n_e, when the extraordinary ray travels perpendicular to the optical axis. In general:

$$n_e(\theta) = \frac{n_o n_e}{\sqrt{n_o^2 sin^2(\theta) + n_e^2 cos^2(\theta)}} \tag{5.1}$$

Phase-matching is achieved by adjusting θ such that $n_o(\omega) = n_e(\theta, 2\omega)$. Recalling the relationship $\Delta k = \frac{2\omega}{c}[n(\omega) - n(2\omega)]$ established earlier in Section 2.4, when $\Delta k = 0$, the condition for the sinc function to attain its maximum is satisfied. In reference to Figure 5.3, the BBO phase-matches when it is rotated to 78° and 168° (relative to an arbitrary angle) corresponding to the two crests. The SHG intensity varies as a function of θ with a period of 90° so that if the HWP is rotated another 180°, the wave pattern in the figure should repeat itself. This shows that it is possible to vary Δk, and even reduce it to zero, by rotating the nonlinear crystal about the beam axis. From this experiment, one can easily appreciate the criticality of phase-matching in efficient second harmonic generation.

5.3 Selecting a Microscope Objective Lens for SHG Imaging

The intensity of SHG signal is measured as a function of depth in the BBO crystal near the crystal surface (zero distance corresponds to the initial position where the objective lens is just in contact and the focal point is inside the crystal. With increasing distance, the focal point gets progressively closer to the crystal surface, corresponding to a decreasing depth in the crystal). Four different microscope objectives were tested in both the transmission and reflection modes.

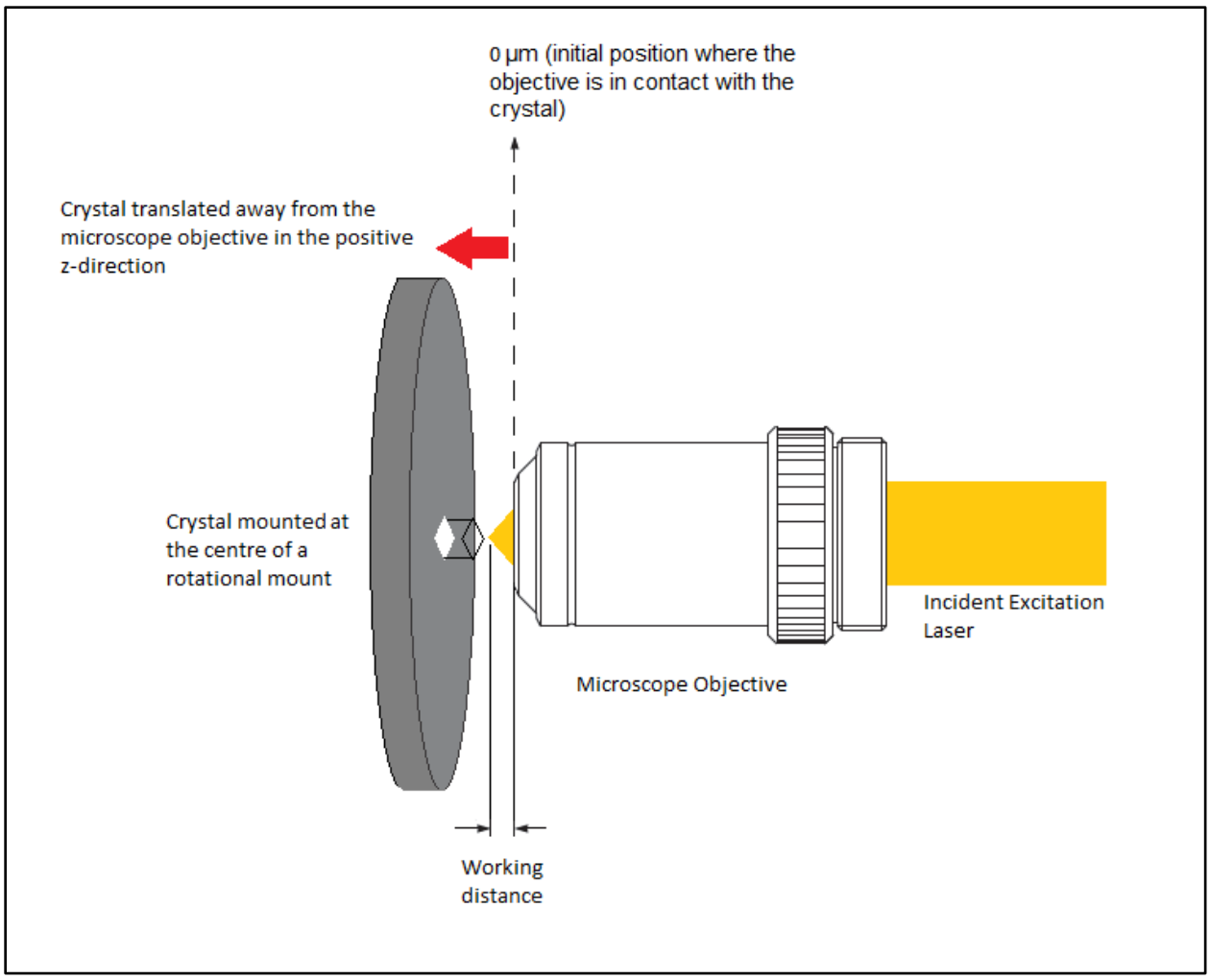

Figure 5-4. Diagram showing the experimental setup and procedure for measuring the SHG signal as a function the distance between surface of the microscope lens and the crystal surface.

5.3.1 Transmission Mode

For all four objective lenses, the BBO crystal was manually translated away from the objective lens in steps of 50 µm (see Figure 5-4), with the exception of the 0.90 NA objective, where some measurements were taken in 10 µm intervals to obtain a more accurate trend.

The 25x/ 0.50 NA Objective

Figure 5-5 shows the graph of the SHG intensity as a function of the crystal's relative distance away from the surface of the 25x/0.50 NA microscope objective. The plot shows that the SHG intensity is normally distributed with the signal peak at the air-crystal interface. Starting at z-

distance of 0 µm, the focal point of the excitation laser is at a depth inside the crystal. As the distance is increased, the focal point gets closer to the crystal surface until the peak at 1300 µm (as annotated in Figure 5-5, which corresponds to the working distance of the microscope objective (WD of 1.30 mm). Beyond the air-crystal interface, the signal intensity drops off rapidly as the focus of the laser is no longer inside the crystal volume.

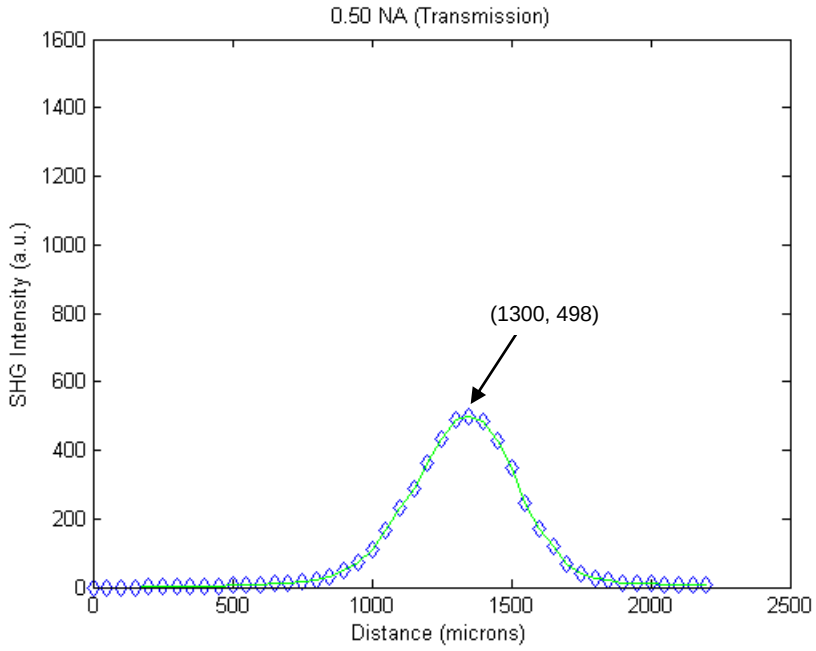

Figure 5-5. SHG signal recorded as a function of z-distance with the 0.50 NA objective in transmission mode.

The SHG peak observed at air-crystal interface is explained by the Gouy phase-shift described earlier in Section 2.6. This results in phase-shifts of both the laser and the SHG electric fields as they pass through the focal region. However, the phase of the SHG polarisation is shifted twice as much as the propagating light. This means that the SHG light generated before and after the focus are out-of-phase to each other, resulting in cancellation of the SHG signals in the uniform array inside the bulk of the crystal, i.e. at a distance of many Rayleigh ranges from the surface of the sample [17]. A large SHG signal (observed as the SHG peak) occurs only when beam is focussed near the front or the back surface of the crystal.

The value of the full width at half-maximum (FWHM) of the SHG signal peak is uniquely related to two important properties of the beam: the beam radius (w_0) and the Rayleigh range (z_R), which is effectively the range at which SHG is generated in the medium. Hence, the FWHM

value is found by modelling the SHG curve with a Gaussian fit using the MATLAB software to calculate the values of w_0 and z_R.

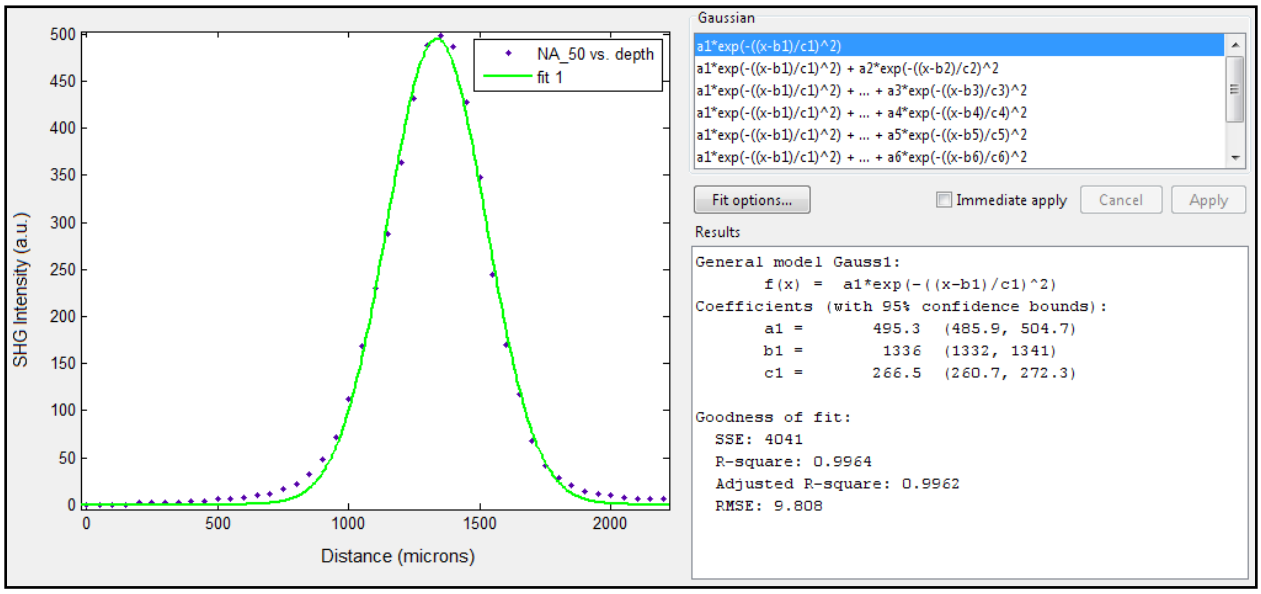

Figure 5-6. MATLAB output of the Gaussian fit of the SHG peak.

From the Gaussian fit and the Gaussian formula generated by MATLAB as shown in Figure 5-6, the SHG signal peak is found to be 14.2 a.u. with a FWHM of 375 µm. Based on the relationships $w_0 = \frac{0.61\lambda}{NA}$ and $z_R = \frac{n\pi {w_0}^2}{\lambda}$, the beam radius and the Rayleigh range are calculated to be 1.26 µm 7.78 µm, respectively. These values are comparable to the beam parameters quoted in a similar SHG imaging study by Stoller et al in 2003 [17].

The 40x/ 0.65 NA Objective

With the 40x 0.65 NA objective, the SHG signal peak has FWHM of 140 µm, a calculated beam waist of 9.67 µm and Rayleigh range of 4.60 µm. In Figure 5-7, the SHG peaks when the distance between the crystal surface and the objective is 450 µm. This value coincides with the 470 µm working distance of the microscope objective.

By comparing Figures 5.5 and 5.7, the signal peak obtained using the 0.65 NA objective is significantly narrower and higher than the one obtained from the 0.50 NA objective. This result is expected as an objective lens with a higher numerical aperture is able to focus the laser light down to a smaller focal point, resulting in a higher intensity incident on the BBO crystal. As the efficiency of SHG is proportional to the square of the excitation flux intensity, a stronger SHG signal is detected by the PMT.

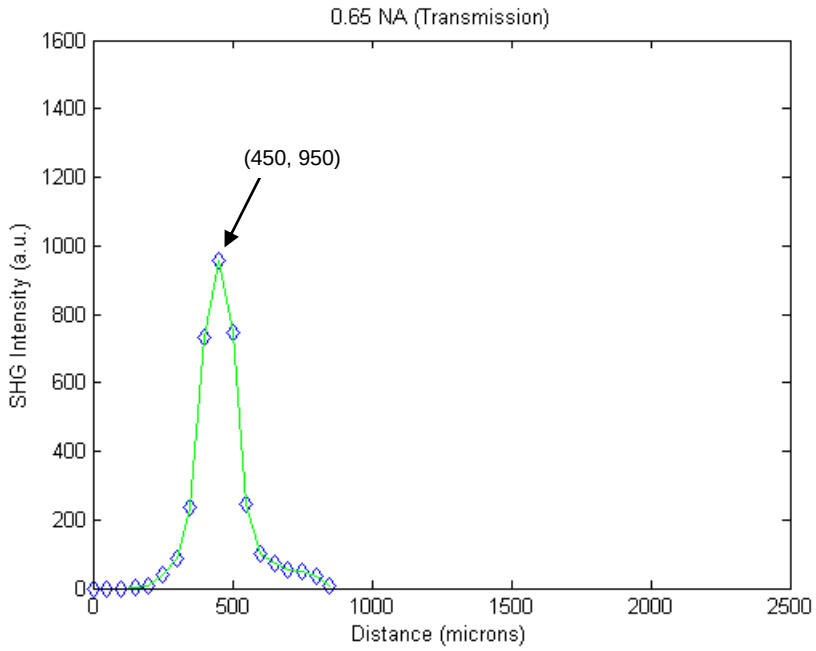

Figure 5-7. SHG signal recorded as a function of z-distance with the 0.65 NA objective in transmission mode.

Despite the considerably higher SHG intensity it produced, it must be stressed that the image penetration is greatly limited by its short working distance. Consequently, this 0.65-NA objective is deemed unsuitable for SHG microscopy.

Recalling the nonlinear response of the PMT at intensities above 560 a.u., the SHG peak in the figure is slightly underestimated. If the nonlinearity is taken into account, the true SHG intensity is calculated to be 1030 a.u.

The 80x/ 0.80 NA Objective

Figure 5-8. SHG signal recorded as a function of z-distance with the 0.65 NA objective in transmission mode.

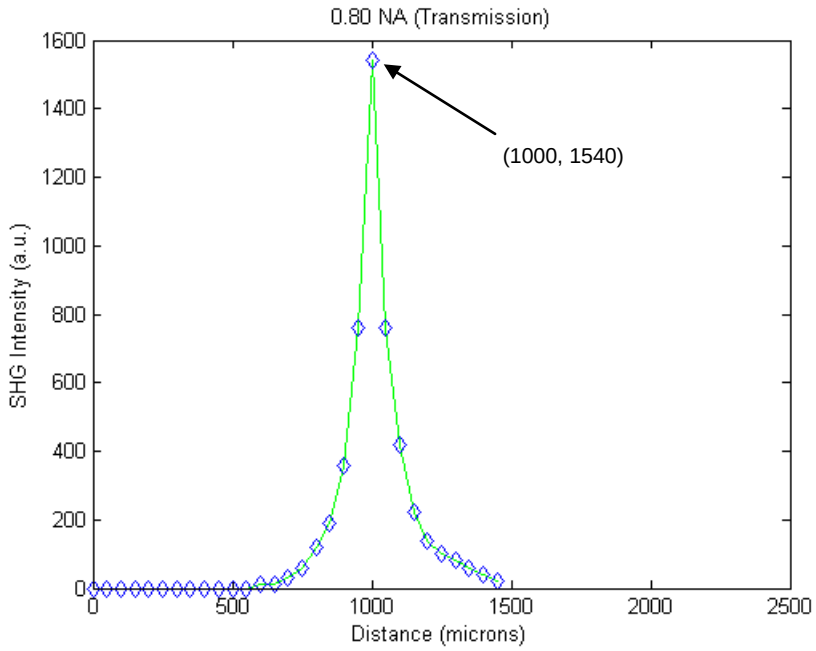

From Figure 5-8, the SHG peak obtained using the 50x/0.80 NA microscope objective has FWHM of 93 µm, beam waist of 7.85 µm and Rayleigh range of 3.04 µm. The signal strength has further increased and the peak has become even narrower, which is consistent with the explanation given in the previous section.

At such high SHG intensities and knowing that the sensitivity of the PMT decreases progressively beyond intensities of 560 a.u., the height of the SHG peak in the figure is significantly underestimated. Accounting for the nonlinear response of the PMT, a corrected SHG intensity of 2510 a.u. is calculated.

The 100x/ 0.90 NA Objective

The 100x/ 0.90 NA objective has generated a SHG peak with FWHM of 36 µm, beam waist of 6.98 µm and Rayleigh range of 2.40 µm. In comparison with the other graphs, Figure 5.8 shows a much narrower SHG peak. However, the height of the peak is slightly lower than the one obtained using the 0.80 NA microscope objective.

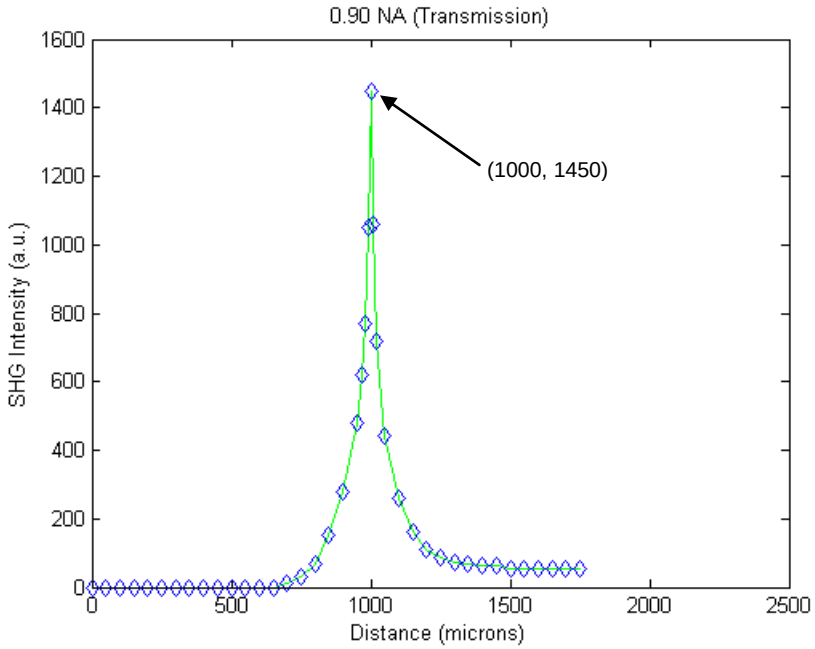

Figure 5-9 SHG signal recorded as a function of z-distance with the 0.65 NA objective in transmission mode.

This can be explained by the equation $NA = n \sin\theta$, there the NA of an objective is proportional to the angular aperture, θ, of the cone of light emitted from the objective. As illustrated in Figure 5-9, the SHG light generated by the 0.90 NA objective will be emitted from the crystal with a larger angular distribution than that of the 0.80 NA objective. Since the SHG signal is not collimated before reaching the PMT and due to the small diameter of the PMT's detector head (5 mm), some of the signal generated by the 0.80 NA objective may hit the inner wall of the detector or miss it altogether as illustrated in Figure 5-10. When less of the signal is collected, the SHG peak will drop.

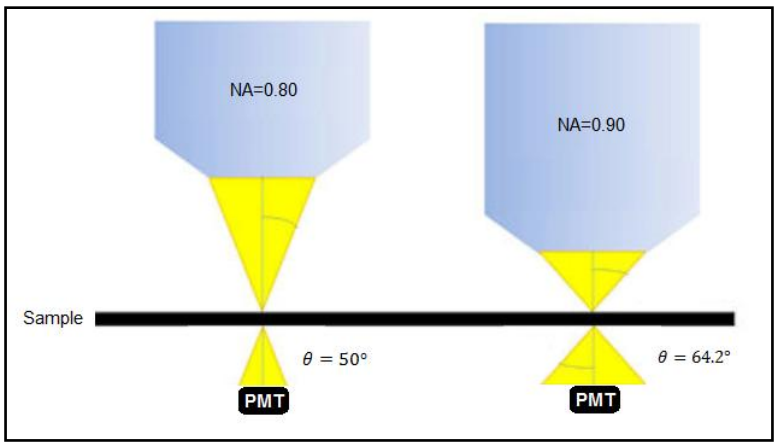

Figure 5-10. Effect of numerical aperture on the angular aperture of microscope objectives.

Figure 5-11 overlays the four SHG peaks on the same axes. The dashed line at z-distance 0 µm is the relative position of the crystal surface from the front apertures of the objectives. Generally in microscopy, one aims to obtain the highest possible image resolution with minimal compromise on the image quality.

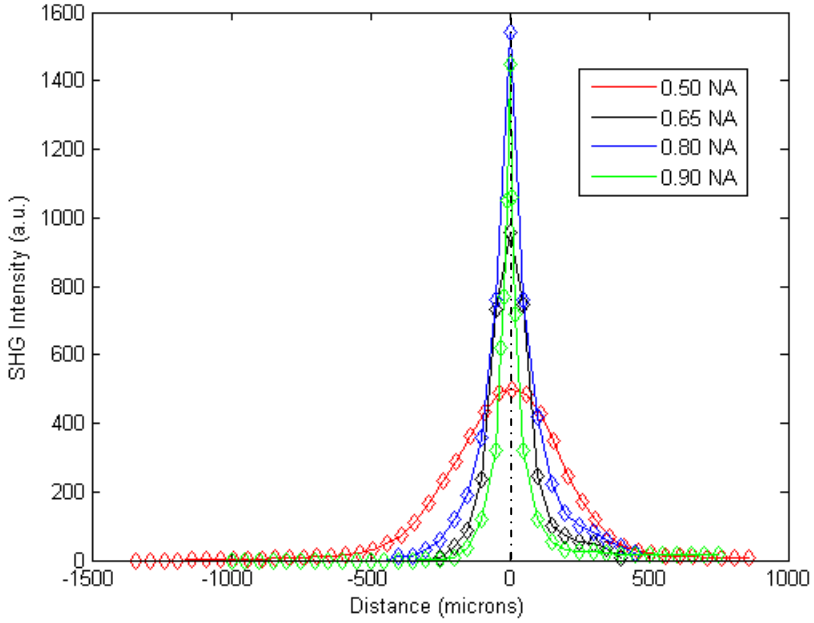

Figure 5-11. Comparison of the SHG peaks obtained in transmission using the four microscope objectives.

From Figure 5-11, the 100x/.90 NA objective (green curve) is clearly the one with the narrowest SHG peak, which means that it has a superior depth resolution over all other objectives. However, it produces a weaker SHG signal then the 0.80 NA microscope objective (represented by the blue curve), which can potentially mean a reduction in the image contrast. Thus, the 50x/0.80 NA objective is considered the most suitable in this project and is selected for collagen imaging in Section 5.5.

Microscope Objective (power/NA)	Peak SHG Signal (a.u.)	FWHM of SHG Signal (μm)	w_0 (μm)	z_R (μm)	WD (mm)
25×/0.50	498	375	1.26	7.78	1.30
40×/0.65	956 (1030)	140	0.967	4.60	0.47
50×/0.80	1540 (2510)	93	0.785	3.04	1.00
100×/0.90	1450 (2346)	36	0.698	2.40	1.00

Table 5-1. Important features of the microscope lenses and their resulting beam parameters. The values in brackets are calculated from the measured SHG intensities taking into account the nonlinear response of the PMT to stronger light stimuli.

Table 5-1 gives a summary of the important features of the laser beam used in the experiments and a comparison of the SHG signals produced from different microscope objectives in transmission mode. Because the PMT has a nonlinear response at above approximately 560 a.u., an estimate of the true peak signal needs to be calculated from the measured value. The bracketed SHG signal values have been corrected to compensate for the nonlinearity.

Reflection Mode

The same experiments from the previous section are repeated for the same microscope lenses in reflection mode, where only the backward component of the SHG signals are collected.

The general shape of the SHG peaks obtained in reflection mode are similar to those that are collected in transmission mode for all four microscope objectives, however, their intensities are relatively much lower. This indicates that during the SHG process, most of the frequency-doubled light will propagate in the forward direction and only a small fraction is emitted backwards. These results are in accordance with past studies where typically, depending on the

scattering properties and the structural orientation of the sample, 80% to 90% of the total SHG signal is found to be forward-propagating [18,31,34]. However, with F_{SHG}/B_{SHG} ratios of between 30.0 and 35.1, the backward SHG signals are much lower than expected for all four microscope objectives. This can be attributed to a potential flaw in the microscope design. From Figure 5-11, it can be seen that the backward SHG signal has to travel a much longer path then the forward SHG before reaching the PMT, which can potentially result in a reduction in the reflected signal.

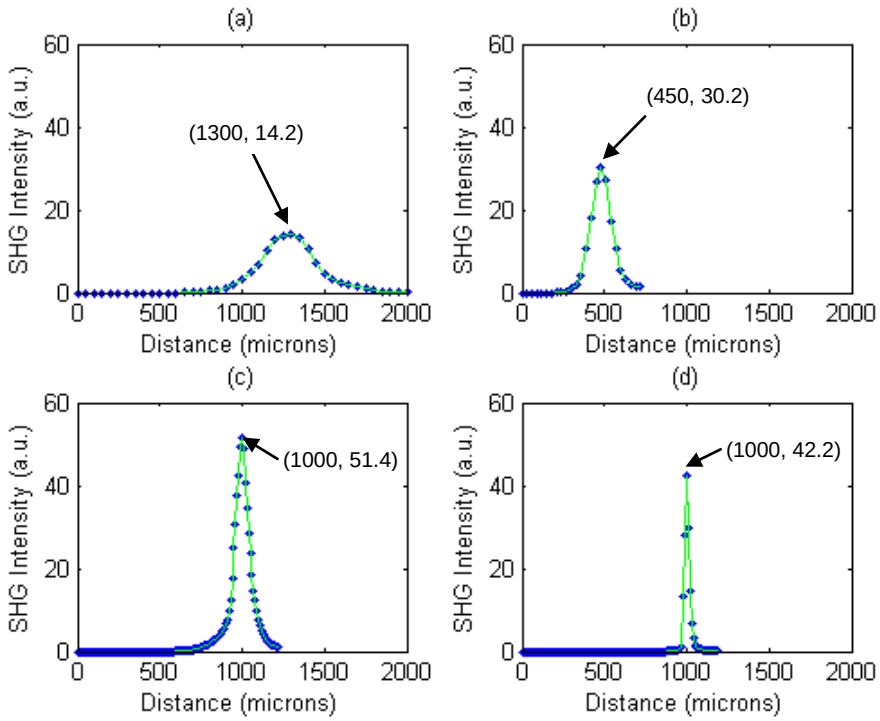

Figure 5-12. Plots of the SHG peaks as a function of z-distance by different objectives in reflection mode.

From the FWHM of the peaks, the spot size and the Rayleigh range resulting from each of the four objectives are calculated and tabulated in Table 4-2. From Figure 5-12, the peaks are located at 1300 µm, 450 µm, 1000 µm and 1000 µm for the 0.50 NA, 0.65 NA, 0.80 and 0.90 NA objectives, respectively, which are all in agreement with the working distances of the microscopes and with the values obtained earlier in transmission mode.

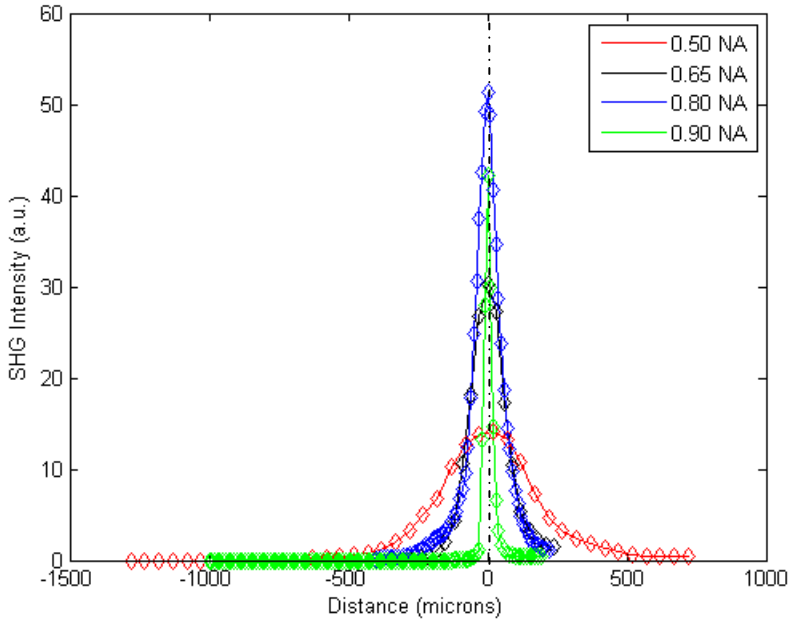

Figure 5-13. Comparison of the SHG peaks obtained in reflection mode using the four microscope objectives.

The heights of the SHG peaks in Figure 5-13 share the same pattern as the ones obtained in transmission mode. Again, the 50x/0.80 NA objective is deemed the most suitable for SHG imaging in reflection mode.

Table 5.2 summaries all the important features of the SHG peaks obtained from the four objectives in reflection mode.

Microscope Objective (power/NA)	Peak SHG Signal (a.u.)	FWHM of SHG Signal (μm)	w_0 (μm)	z_R (μm)	WD (mm)
25×/0.50	14.2	379	1.26	7.78	1.30
40×/0.65	30.2	142	0.967	4.60	0.47
50×/0.80	51.4	91	0.785	3.04	1.00
100×/0.90	42.2	35	0.698	2.40	1.00

Table 5-2. Important features of the microscope lenses and their resulting beam parameters.

5.4 Polarisation Measurements

To study the dependence of the SHG signal intensity on polarisation, a half-wave plate (HWP) is mounted on a rotational mount placed between Mirrors 1 and 2 (see Figure 3.1). The wave-plate is then rotated manually from an arbitrary reference angle in regular intervals and the relative SHG intensities recorded at each angular position.

The experiment is carried out using a 570 µm slice of chemically modified bovine pericardium. The tissue is laid flat on the back surface of a standard 150 µm cover slide and mounted on a XYZ-translation stage within 1 mm of the front aperture of the 0.80 NA microscope objective. The PMT is placed in position for imaging in reflection mode. A certain spot in the tissue with a strong SHG signal is then chosen by finely adjusting the tissue position with respect to the incident beam. Because the tissue is exposed to air, the HWP is rotated in intervals of 10° to shorten the duration of the experiment and, and therefore, to prevent the drying out of the tissue. To make sure that the signal variations actually arise from structural differences within the sample and are not simply image artefacts, a number of 'depth-scan' experiments are performed on different points on the sample.

The intensities of the SHG signal resulting from each turn of the HWP over an entire revolution is shown in Figure 5-14. The fact that the three sets of experimental data each have a different phase relative to the others (observed as the different positioning of the crests and troughs) eliminates the possibility that signals are resulting from signal artefacts. This is further reinforced by the periodic pattern observed every 180°, which coincides with the rotation of the HWP.

Although the structure of the bovine pericardium is unknown so no association between its fine structure and the SHG intensities could be made, the detection of variations in signal intensities is a promising indication that the SHG microscope is polarisation-sensitive to the tissue structure. This means that with some modifications, the microscope could potentially be upgraded to a polarisation-resolved microscope.

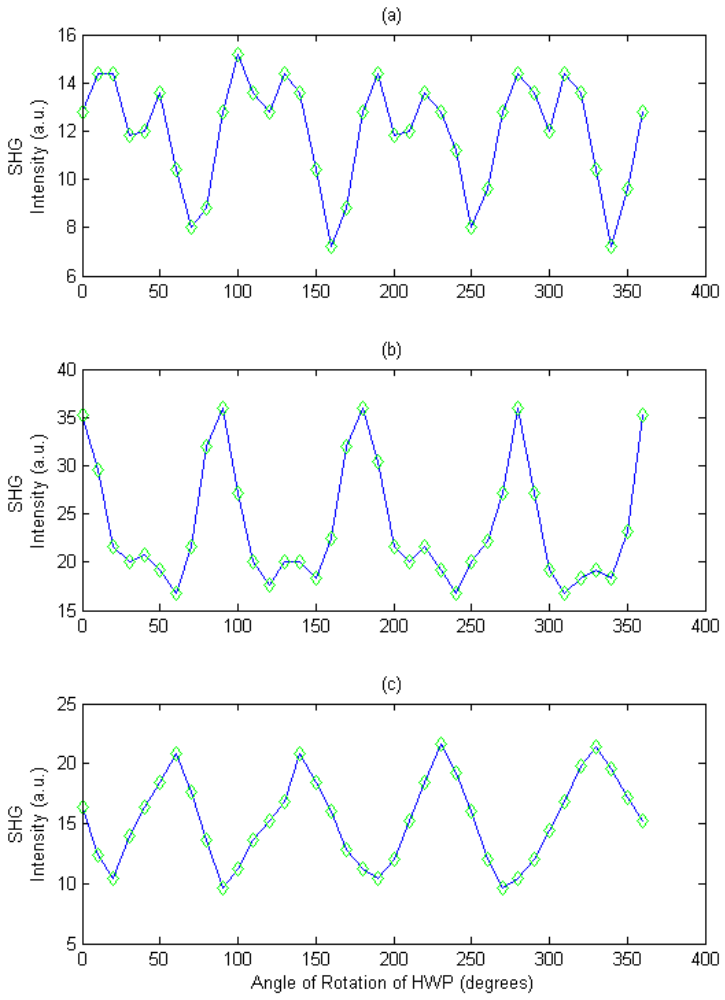

Figure 5-14. SHG signal as a function of the rotational angle of the HWP at three difference positions in the tissue sample.

Conventional SHG microscopy utilises variations in image intensity for simple visualisation of fine collagen structure but provide little information on the orientation of individual fibres. Past studies have found that the degree of parallel and anti-parallel orientation of neighbouring collagen fibres can give rise to variations in SHG intensity [17,22,39]. This finding is supported by the theory that two neighbouring fibres oriented in the same direction will generate SHG that are in phase with each other, resulting in an enhanced SHG signal. For two neighbouring fibres pointing in opposite directions, their SHG signals will undergo destructive interference and cancel out, resulting in a weaker signal [12,22]. While this technique allows information to be

obtained from a group of fibres, as each individual signal results from the contribution of a number of neighbouring fibres, the ensemble-averaged measurement makes it impossible to determine the orientation of single fibres.

Recently, there has been increasing interest in polarisation-resolved microscopy, which is capable of detecting the orientation of individual fibres [4,40]. By aligning the laser polarisation with the long-axis of a collagen fibre and rotating through 180°, the intensity measurements as a function of laser polarisation can be used to determine the fibre orientation.

5.5 2-Dimensional Collagen Data Acquisition

The experimental procedures in this section is largely the same as those described in Sections 5.3.1 and 5.3.2 with the exception that a 570 µm-thick bovine pericardium section is used in place of the BBO crystal and a 50x/ 0.80 NA objective is used. The relative starting position of the sample from the microscope is also different. The same spot in the tissue is imaged in both the transmission and reflection modes.

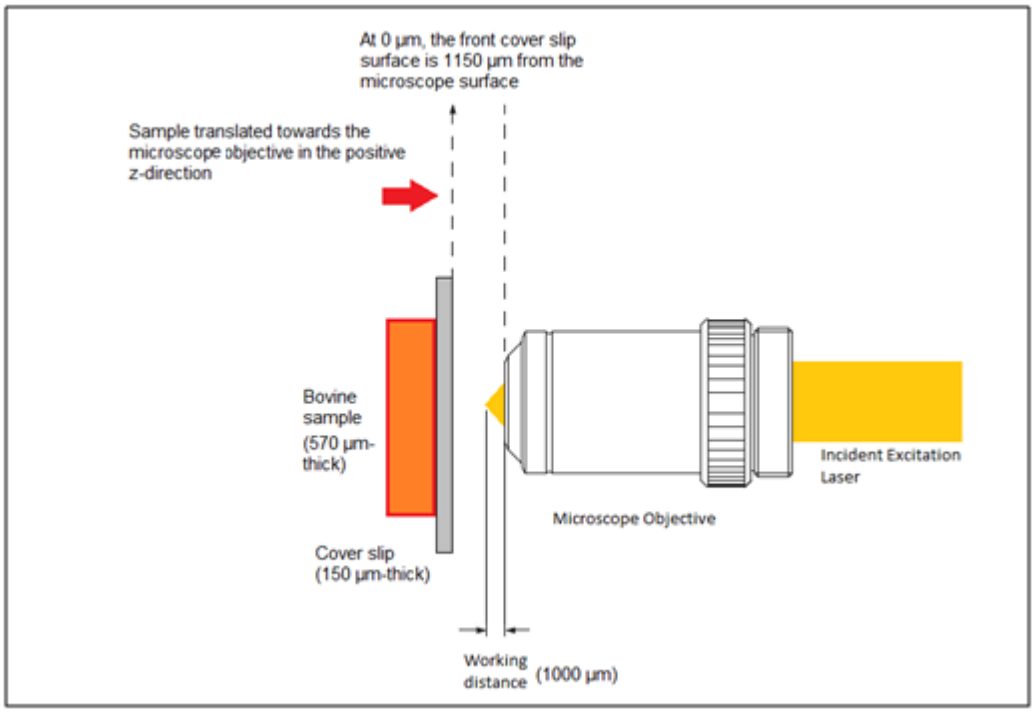

Figure 5-15. Diagram showing the experimental setup and procedure for measuring the SHG signal as a function the distance between surface of the microscope lens and the bovine tissue.

A set of measurements is first made in transmission mode to record the SHG signal starting with at 0 µm (which corresponds to the front surface of the objective at 1150 µm from the microscope cover slip) as shown in Figure 5-15. Note that because the working distance of the objective is 1 mm, the excitation beam is in front of the front surface of the glass cover slip. The sample is then slowly moved towards the objective in steps of 50 µm up to a z-distance of 800 µm (when the cover slip surface is 350 µm from the objective) to scan at increasing depths of the sample until a SHG signal is no longer detected. Once this is completed, the PMT is repositioned for imaging in reflection mode and the SHG signals are collected as the sample is translated back from 800 µm to 0 µm.

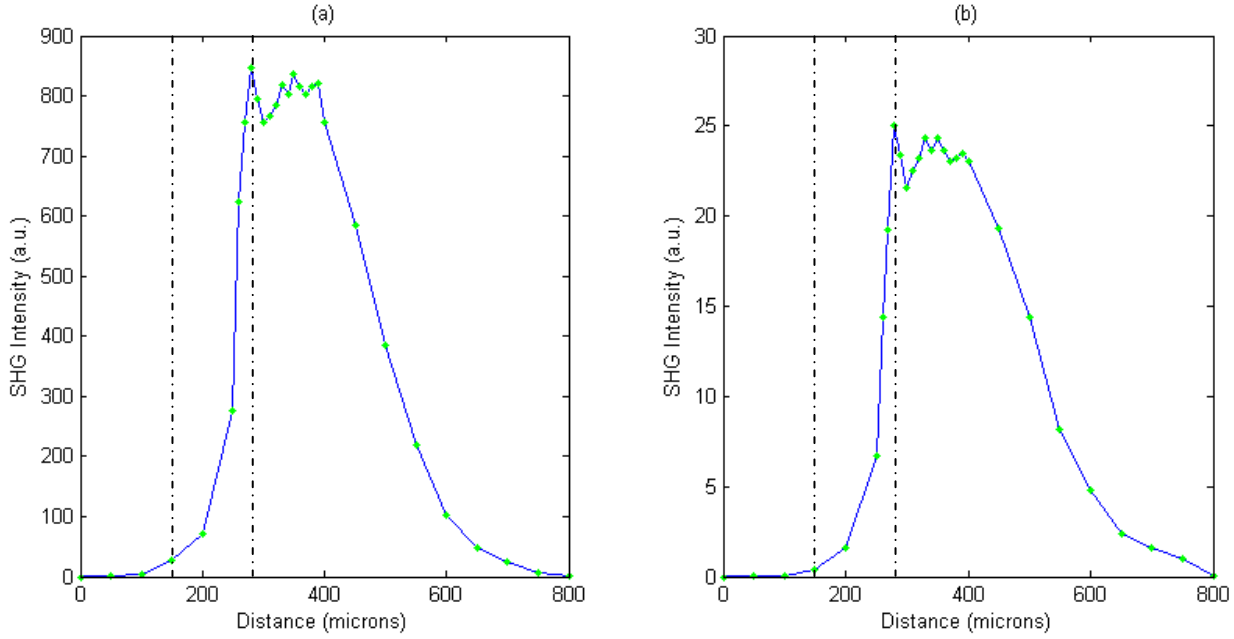

Figure 5-16. SHG signal as a function of depth in a) transmission mode, and b) in reflection mode, in the tissue sample. The distance between the two dashed lines is the thickness of the cover slip.

Figure 5-16 (a) shows the SHG intensity recorded in transmission mode and (b) in reflection mode. The dashed line at 280 µm represents the position of the back surface of tissue sample At distances of 0 µm to 150 µm, the beam focus is in the air so minimal signal is recorded as expected. Between 150 µm and 300 µm, the focus is found within the cover slip. Again, little signal is expected as glass is not non-centrosymmetric. The plots show that as the sample is moved closer to the focal point, the SHG signal initially increases gradually. But as it comes into

close proximity to the air-tissue interface, there is a rapid increase in the signal and a small spike in signal intensity at approximately 280 µm. Beyond the tissue surface, the signal intensity drops back a little and form a plateau as the focal point moves deeper into the sample.

Between 280 µm and 400 µm, the system detected a similar pattern of signal variations in both modes. As each individual collagen fibre has a cross-section diameter of typically 0.5 µm to 3 µm, the signal variations detected at a resolution of 5 µm is a promising sign that the system is capable of extracting structural information from collagen samples. However, to visualise each individual collagen fibre, a higher imaging resolution is required.

The drop in SHG intensity beyond 400 µm (depth of 120 µm in the tissue) can be explained by the limit in penetration depth of SHG microscopy in general. As discussed earlier in Chapter 3, the excitation laser experiences multiple scattering and absorption events as it propagates through the tissue sample. These attenuating events can substantially reduce the number of incident ballistic photons, which explains why recorded the SHG signal dropped rapidly with increasing imaging depth.

The typical penetration limit of SHG microscopy with a Ti:sapphire laser is approximately 250 to 300 µm. Using the 1032 nm laser, SHG signals of considerable intensities are detected at 320 µm and beyond, which suggests that the microscope built in this project has superior penetration depth over the conventional Ti:sapphire powered SHG microscope.

5.6 Discussion

The maximum image resolution of the preliminary microscope design is primarily limited by manually translating the sample as a means of scanning the beam across the sample. With a smallest division of 10 µm on the micrometer drive, the finest resolution achievable is 10 µm. Although this level of precision is quite good for a manual stage, it fails to provide the sub-micron image resolution required for imaging individual collagen fibres 500 nm to 3 µm. To achieve higher resolutions, the laser beam needs to be continuously raster-scanned across the sample and the corresponding SHG signals collected at a rapid rate. Scanning the beam over the biological sample also significantly reduces tissue damage as the energy of the beam is spread over a much larger area.

The resolution of the actual SHG intensities or the “1-D images” is governed by, ω_0, or the focussed spot size. From Tables 5.1 and 5.2, the resolution of the SHG microscope is 1.26 µm when the 25x 0.5 NA microscope objective is used, and 0.698 µm when the 100x 0.90 NA objective is employed.

One practical issue encountered throughout the experiments is the need to keep switching the light, and consequently, the PMT on and off in between each measurement. While all lights in the room need to be turned off during SHG signal acquisition, they need to be turned back on for changing the translation stage position, or the changing the rotation of the crystal or HWP with great precision. This light is sufficient to saturate the PMT and to render it unresponsive to light stimuli for a short period of time so the PMT must be turned off before the room is lit. The need to repeatedly turn the lights and the PMT on and off significantly lengthens the time required for each set of experiment. This issue can easily be solved by implementation of an automated system for scanning the beam on the sample, and the use of motorised rotational stage for angle tuning the BBO crystal and the HWP in a light-tight casing.

Another practical issue is the mounting and positioning of the PMT. The mass and size of the second PMT used in this project are more than five times larger than standard PMT modules. Due to the difficulty of mounting the PMT on a stand, the PMT is simply placed on a platform and secured by its own weight. To switch between imaging modes, much time and effort is required every time to move and adjust the positions of the platform and the PMT. Ideally, two compact PMT modules should be used for the simultaneous image acquisition in the transmission and reflection modes. This will allow the ratio of the forward- and backward-propagating SHG intensity to be calculated and used as a measure of the degree of organisation in the sample.

5.7 Summary

The SHG microscope has been successfully implemented for basic biological imaging. A linear relationship between the SHG signal and the square of the excitation intensity has been established experimentally. The phase-matching condition for efficient SHG conversion has also been realised by angle-tuning a BBO crystal. A suitable microscope objective has been chosen for the microscope to optimise the SHG signal intensity. With the coupling of that objective lens,

the microscope has demonstrated its ability to detect structural variations in the sample as a function of the laser polarisation and the depth within the tissue.

Chapter 6. The Improved Microscope Design

One major flaw in the preliminary SHG microscope design is that all the optics are mounted horizontally on the optical table, which means that the laser is also propagating horizontally and the sample needs to be held vertically in a sample holder. This arrangement poses several issues in the experiments. Firstly, the sample must be held in a sample holder and cannot simply be placed horizontally on top of a secure sample stage. Secondly, the microscope objectives are not designed to be used horizontally. Weighing a substantial 285 g and only being supported at one end, it puts a considerable amount of stress on the delicate xy-translational mount that holds it. The horizontal mounting also means that dipping and immersion objectives, typically with longer working distances, cannot be used. In the modified microscope, the objectives are held upright as in conventional microscopy.

Another important limitation in the microscope is the lack of an automated scanning system. In the new design, a pair of galvanometric mirrors is implemented to scan the laser beam in the z- and y- directions across the sample for 2D image acquisition.

In the preliminary setup, the SHG light is not focussed before signal collection, which means a significant amount of useful signal could potentially be lost before reaching the PMT. A second microscope objective is now added behind the sample to act as a condenser. If positioned correctly, it should collect all SHG signal generated at the focal volume and relay it directly to the PMT for detection.

Diagram 6-1 shows the implementation of the new microscope design. For added stability, the entire microscope is now mounted on cage mounts. Unfortunately, there is insufficient time to test out the modified microscope and to evaluate its supposedly improved imaging capabilities.

From the laser output, the beam is first sent upwards by Mirror 1 and is then collimated by the same telescopic system employed in the preliminary setup to incident on the pair of galvanometric mirrors. As both mirrors are only millimetres wide, special care is taken to make sure that the laser beam does not get clipped near the mirror edges. From the galvanometric scanners, the beam is reflected 45° off Mirror 2 onto the back aperture of a scan lens.

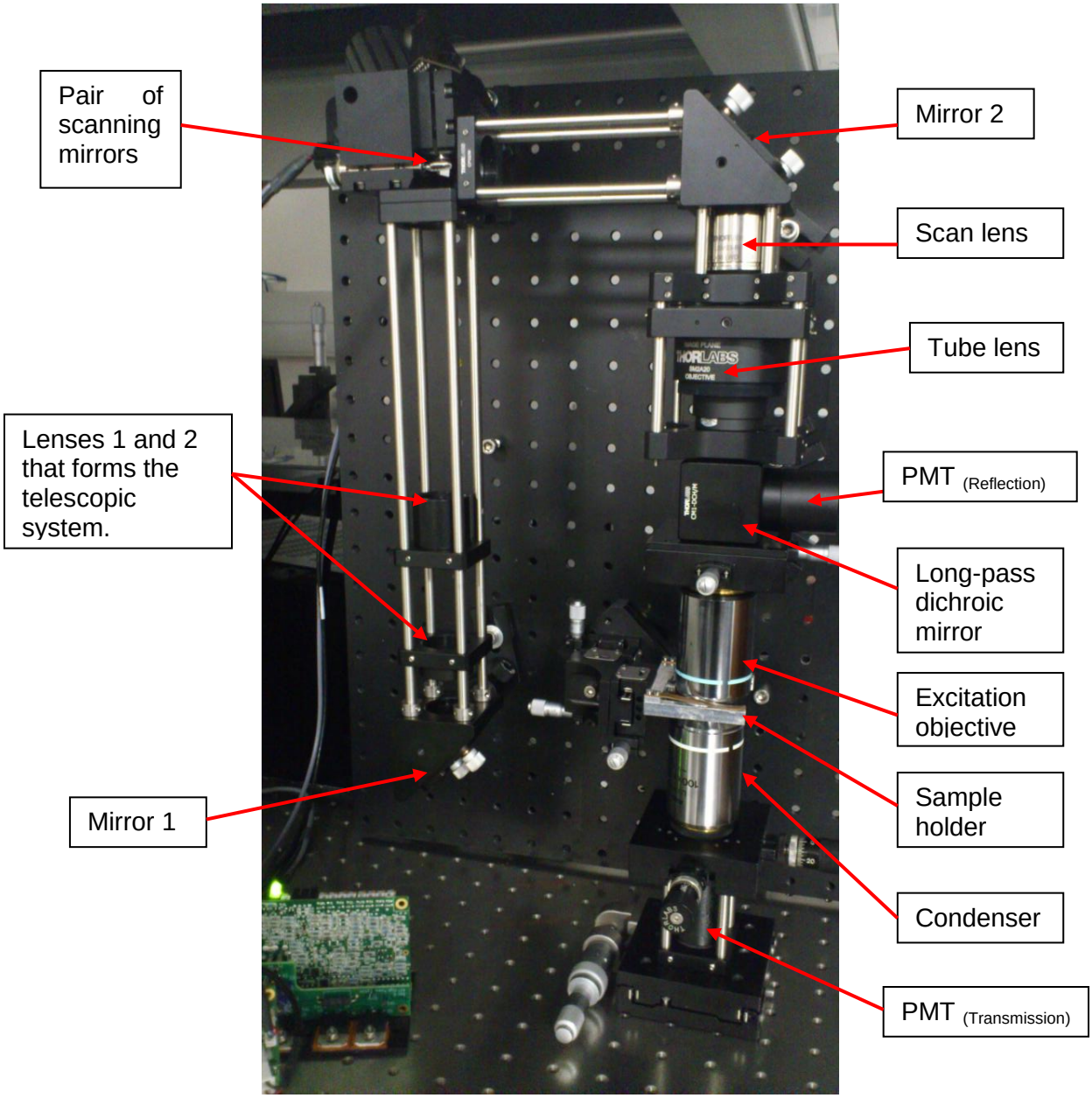

Figure 6-1. Photograph of the improved SHG microscope. The input of the excitation laser is off the photo, to the left of Mirror 1. The PMT modules will be fitted once they become available.

To make sure that the entire scanning beam is collected by the microscope objective at all times, a scan and lens tube combination consisting of a Thorlabs (LSM03-BB) scan lens and a Thorlabs (ITL200) infinity-corrected tube lens is used. Coupled to the scan lens, the tube lens is

used to relay the scan plane of the laser scanning imaging system onto the back aperture of the 50×/0.80 NA microscope objective.

The beam is then sent through a long-pass dichroic mirror and through the 50×/0.80 NA microscope objective to be focussed onto the region of interest in the sample. The sample is placed on a sample stage with freedom of movement in all directions so that any specific point in the sample can be lined up with the beam for imaging.

When operating in transmission mode, the 100×/0.90 NA microscope objective is used as a condenser to collect all light (SHG light as well as the fundamental light) originating from the focal volume. The SHG signal, which is collimated by the objective, will reach the PMT detector with minimal loss while the fundamental 1032 nm light is filtered out by the IR-reflecting mirror.

In reflection mode, the backward SHG signal originating from the focal volume first gets collected and collimated by the 50×/0.80 NA microscope objective. It then gets reflected directly into the PMT for detecting after passing through an IR-filter.

For 2D imaging, the scanning angle and speed of the scanning mirrors are controlled separately by two frequency generators. By synchronising the mirror movements and simply raster scanning the excitation beam across the focal plane, the SHG signal intensity can be measured as a function of beam position. Extrapolation to 3D imaging can be easily achieved by acquisition of 2D images as a function of depth in the sample and reassembling the saved pixels to form an image.

The planned digital acquisition system, consisting of a DAQ and its accompanying LABVIEW software, mentioned in Section 4.1.3 will be implemented for real-time image acquisition. The current computer program only allows the SHG signal to be recorded at a specified sample rate over an indefinite time-interval. The computer codes will need further development for controlling the high-speed scanner and synchronising it with the data acquisition system to get position-specific SHG signals. A matt black box will be built to contain the whole microscope and to block out any ambient light so that future experiments will no longer be required to be performed in total darkness.

Chapter 7. Conclusion/Future Outlook

In this project, a SHG microscope capable of imaging in the transmission and reflection modes have been designed and built to operate at an excitation wavelength of 1032 nm.

The microscope has been successfully implemented to verify the intensity-dependence of SHG and to study the condition of phase-matching with a BBO crystal. Different microscopes were fitted to the microscope and a series of depth measurements were made to determine the size of the beam spot and the resulting Rayleigh ranges. Although the 100×/0.90 NA microscope objective has demonstrated the best depth-resolution as seen by the narrowest SHG peak, at such a high numerical aperture, the SHG intensity is compromised. Thus, the objective that produced the tallest SHG peak was chosen and implemented to the microscope for biological imaging. Consequently, the 50×/0.80 NA objective is found to give the best imaging resolution with minimal reduction in the signal intensity.

When used for biological imaging, the microscope has demonstrated its ability to extract polarisation-sensitive information from the modified bovine pericardium sample. It was also able to detect variations in SHG signal intensities at a resolution of 10 μm (limited by the resolution of the translation stage).

An improved SHG microscope, described in Chapter 6, with a scanning unit has been built to make the existing imaging system more practical and user-friendly. There are plans to further develop the microscope to acquire real-time 3D biological images and allow for the simultaneous imaging in the transmission and reflection modes.

Bibliography

[1] New G., *Introduction to Nonlinear Optics*, Cambridge University Press, Cambridge, (2011).

[2] Guyot-Sionnest P., Chen W., Shen Y., *General Considerations on Optical Second-Harmonic Generation from Surfaces and Interfaces*, Phys. Rev. B 33, 8254-8263, (1986).

[3] Yariv A., *Optical Electronics Fourth Edition*, Oxford University Press, USA, (1995).

[4] Yasui T., Takahashi Y., Araki T., *Polarization-resolved Second-harmonic-generation Imaging of Photoaged Dermal Collagen Fiber*, Proc. Of SPIE, Vol. 71831X, (2009).

[5] Prasad P., Williams D., *Introduction to Nonlinear Optical Effects in Molecules and Polymers,* John Wiley and Sons, Inc., USA, (1991).

[6] Boyd R., *Nonlinear Optics Second Edition*, Academic Press, San Diego, (2003).

[7] Shen Y., *The Principles of Nonlinear Optics*, John Wiley and Sons, Inc., New York, (1984).

[8] Hill W. And Lee C., *Light-Matter Interaction: Atoms and Molecules in Exter*nal Fields and Nonlinear Optics*,* Wiley-VCH, Weinheim, (2007).

[9] Franken P., Hill A., Weinreich G., *Generation of Optical Harmonics*, Physical Review Letters **7**(4):118, (1961).

[10] Dood M., *Second Harmonic Generation*, Huygens Laboratorium, Leiden, (2006).

[11] Liu H., Yao J., Puri A., *Second Harmonic G*eneration in BBO by Fe*mtosecond Ti:Sapphire Laser Pulses*, **109**, Issues 1-2 139-144, (1994).

[12] Eimerl D., Davis, L., Graham E., Zalkin A., *Optical, Mechanical and Thermal Properties of Barium Borate*, J. Appl. Phys., **62**, No. 5, p.1968, (1987).

[13] Eckardt R., Byer R., Masuda H., Fan Y., *Absolute and Re*lative *Nonlinear Optical Efficient of KDP, KD*P, BaB_2O_4, $LiIO_3$, $MgO:LiNbO_3$, and KTP Measured by Phase-matched Second-harmonic Generation*, IEEE Journal of Quantum Electronics, **26**, p. 922-933, (1990).

[14] Honma T., Benino Y., Fujiwara T., Sato R., Komatsu T., *Spatially selected Crystallization in Glass by YAG Laser Irradiation*, Journal of Non-Crystalline Solids 345-6, 17-131, (2004).

[15] Lacomb R., Nadiarynkh O., Townsend S., Campagnola P., *Phase Matching Considerations in Second Harmonic Generation from Tissues: Effects on Emission Directionality, Conversion Efficiency and Observed Morphology*, Opt. Comm. 281, 1823-1832, (2008).

[16] Hecht E., *Optics Fourth Edition*, Pearson Education, Inc., San Francisco, (2002).

[17] Stoller P., Celliers P., Reiser K., Rubenchik A., *Quantitative Second-harmonic Generation Microscopy in Collagen*, Applied Optics **42** No.25, (2003).

[18] Taatjes D., Mossman B., *Methods in Molecular Biology,* Vol.319: Cell Imaging Techniques: Methods and Protocols, Humana Press Inc., Totowa, (2011).

[19] Lodish H., Berk A., Lipursky S., Matsudaira P., Baltimore D., Darrell J., *Molecular Cell Biology Fourth Edition*, W.H. Freeman, New York, (2000).

[20] Cox G., Kable E., Jones A., Fraser I., Manconi F., Gorrell M., *3-DimensionI Imaging of Collagen using Second Harmonic Generation*, Journal of Structural Biology 141, 53-65, (2003).

[21] Kim B., Eichler J., Reiser K., Rubenchik A., Da Silva L., *Collagen Structure and Nonlinear Susceptibility: Effects of Heat, Glycation, and Enzymatic Cleavage on Second Harmonic Signal Intensity*. Laser Surg. Med, 27, 329-335, (2000).

[22] Freund I., Deutsch M., Sprecher A., *Connective Tissue Polarity, Optical Second-harmonic Microscopy, Cross-beam Summation, and Small-angle Scattering in Rat-tail Tendon*, Biophys. J. 50, 693-712, (1986).

[23] Lin S., Wu. R, Lo W., Young T., Hsu C., Chen J., Jee S., Dong C., *Evaluating Cutaneous Photoaging by use of Multiphoton Fluorescence and Second-harmonic Generation Microscopy*. Opt. Lett. 30, 2275-277 (2005).

[24] Sahai E., Wyckoff J., Philippar U., Segall J., Gertler F., Condeelis J., *Simultaneous Imaging of GFP, CFP and Collagen in Tumours in vivo using Multiphoton Microscopy*, BMC Biotechnol, 5,14, (2005).

[25] Nadiarykh O., LaComb R., Brewer M., Campagnola P., *Alterations of the Extracellular Matrix in Ovarian Cancer Studied by Second Harmonic Generation Imaging Microscopy*, BMC Cancer, 10:94, (2010).

[26] Lin S., Jee S., Wu R., Lin W., Chen J., Liao Y., Hsu C., Tsai T., Chen Y., Dong C., *Discrimination of Basal Cell Carcinoma from Normal Dermal Stroma by Quantitative Multiphoton Imaging*. Opt. Lett. 31, 2756-2758, (2006).

[27] Dombeck D., Kasischke K., Vishwasrao H., Ingelsson M., Hyman B., Webb W., *Uniform Polarity Microtubule Assemblies Imaged in Native Brain Tissue by Second-harmonic Generation Microscopy*, Proceedings of the National Academy of Science of the United States of America, **100** No. 12, 7081-7086, (2003).

[28] Yasui T., Takahashi Y., Ito M., Fukushima S., Araki T., *Ex vivo and in vivo Second-harmonic-generation Imaging of Dermal Collagen Fiber in Skin: Comparison of Imaging Characteristics between Mode-locked Cr:forsterite and Ti:sapphire Lasers*, Applied Optics **48** No. 10, (2009).

[29] Anderson R., Parrish J., *The Optics of Human Skin*, The Journal of Investigative Dermatology, 77:13-19. (1981)

[30] Bashkatov A., Genina E., Kochubey V., Tuchin V., *Optical Properties of Human Skin, Subtaneous and Mucous Tissues in the Wavelength Range from 400 to 2000 nm*, J. Phys. D: Appl. Phys. 38, 2543-2555, (2005).

[31] Campagnola P., Dong C., *Second Harmonic Generation Microscopy: Principles and Applications to Disease Diagnosis*, Laser Photonics Rev. 5, 13-26, (2011).

[32] Gauderon R., Lukins P., Sheppard C., *Optimization of Second-harmonic Generation Microscopy*, Micron 32, 691-700, (2001).

[33] Carriles R., Schafer D., Sheetz K., Field J., Cisek R., Barza V., Sylvester A., Squier J., *Invited Article: Imaging techniques for Harmonic and Multiphoton Absorption Fluorescence Microscopy*, review of Scientific Instruments 80, 081101, (2009).

[34] Chen X., Nadiarynkh O., Plotnikov S., Campagnola P., *Second Harmonic Generation Microscopy for Quantitative Analysis of Collagen Fibrillar Structure*, Nature Protocols **7** No.4, (2012).

[35] Nikonlenko V., Nemet B., Yuste, R., *A Two-photon and Second-harmonic Microscope*, Mathods 30, 3-15, (2003).

[36] Erkintalo M., Aguergaray C., Runge A., Broderick N., *Environmentally Stable All-PM All-fiber Giant Chirp Oscillator,* Opt. Express 20, 22669-22674 (2012).

[37] Aquergaray C., Broderick N., Erkintalo M., Chen J., Kruglov V., *Mode-locked Femtosecond All-normal All-PM Yb-doped Fiber Laser using a Nonlinear Amplifying Loop Mirror*, Opt. Express 20, 10545-10551, (2012).

[38] Rev E., *Thorlabs PMM01 Amplified Photomultiplier User Guide*, Thorlabs, Inc, USA, (2012).

[39] Roth S., Freund I., *Optical Second-harmonic Scattering in Rat-tail Tendon*, Biopolymers 20, 1271-1290, (1981).

[40] Stoller P, Kim B., Rubenchik A., Reiser K., Da Silva L., *Polarization-dependent optical Second-harmonic Imaging of a Rat-tail Tendon*, Journal of Biomedical Optics 2(2), 205-214, (2002).

Appendix A. LABVIEW Diagram for PMT Data Acquisition

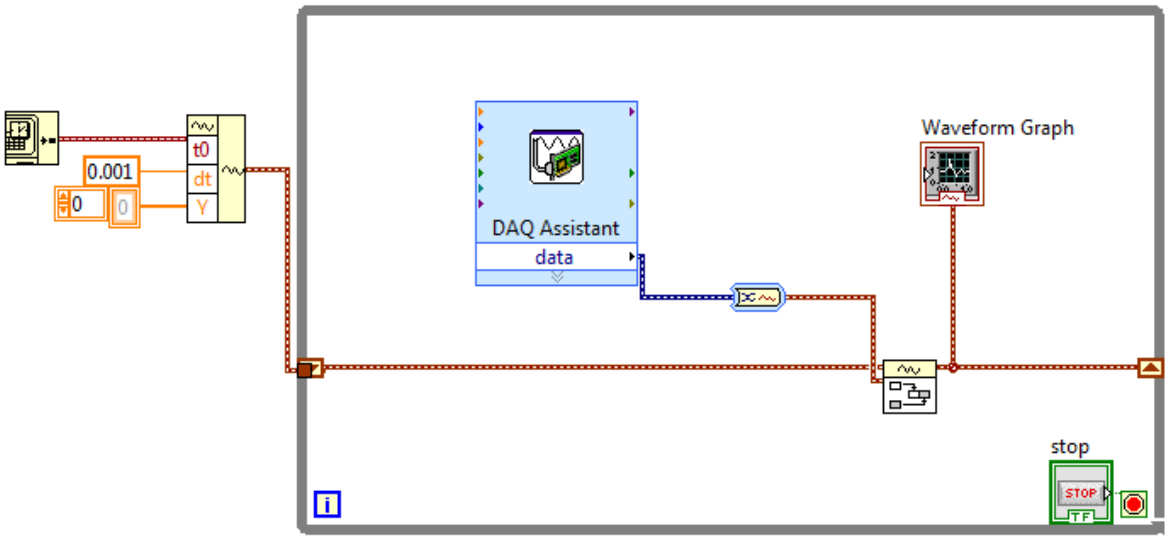

Appendix B. Additional Images of the Preliminary Microscope Design

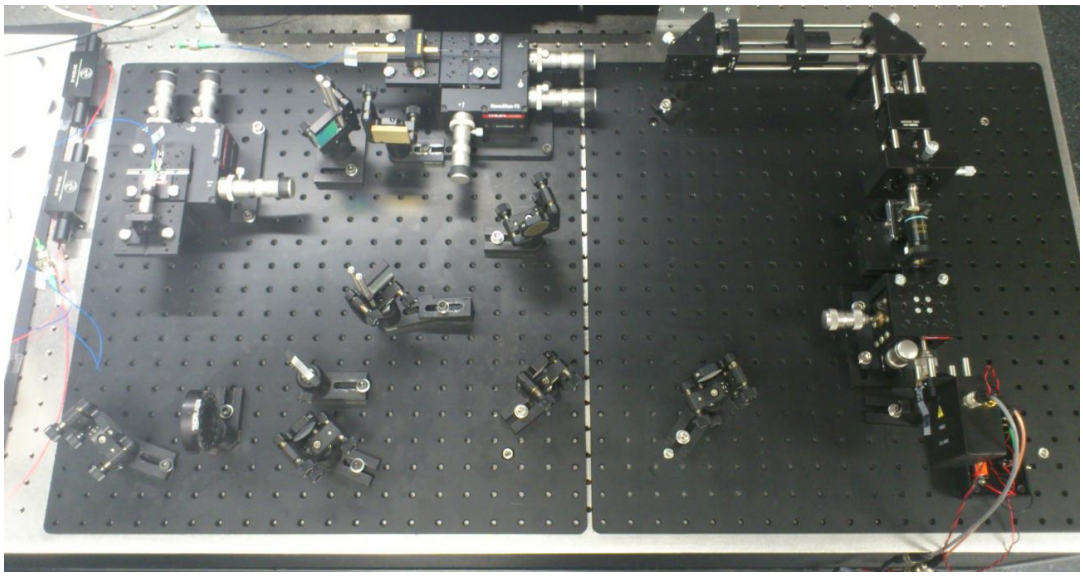

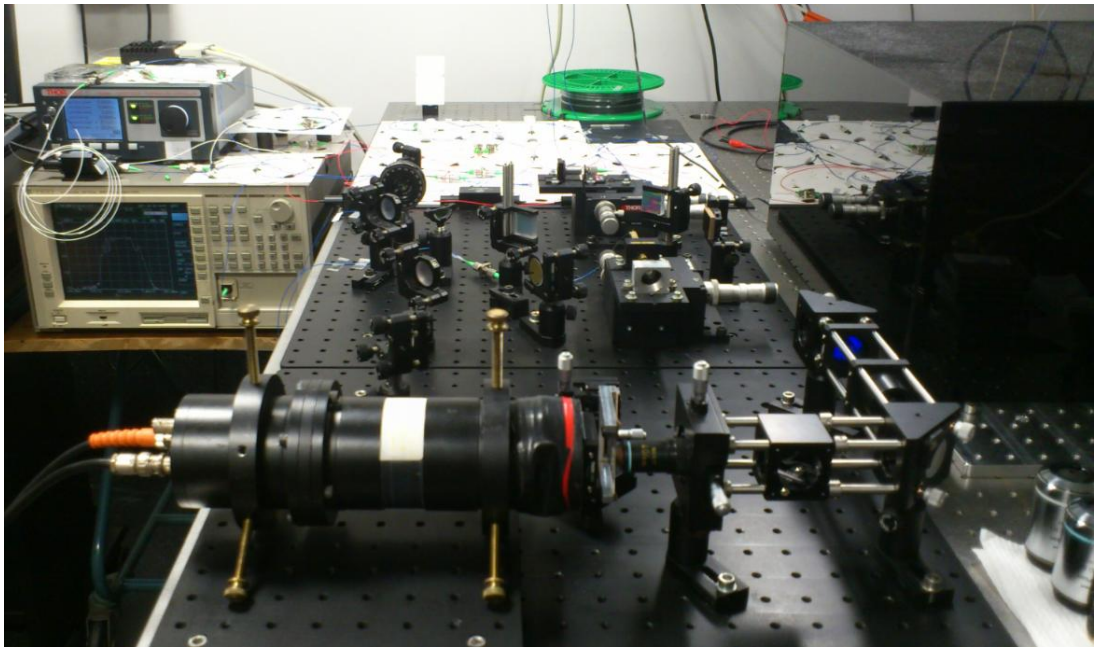

Images of the microscope in transmission mode (top) with the Thorlabs PMT and (bottom) with the EMI PMT

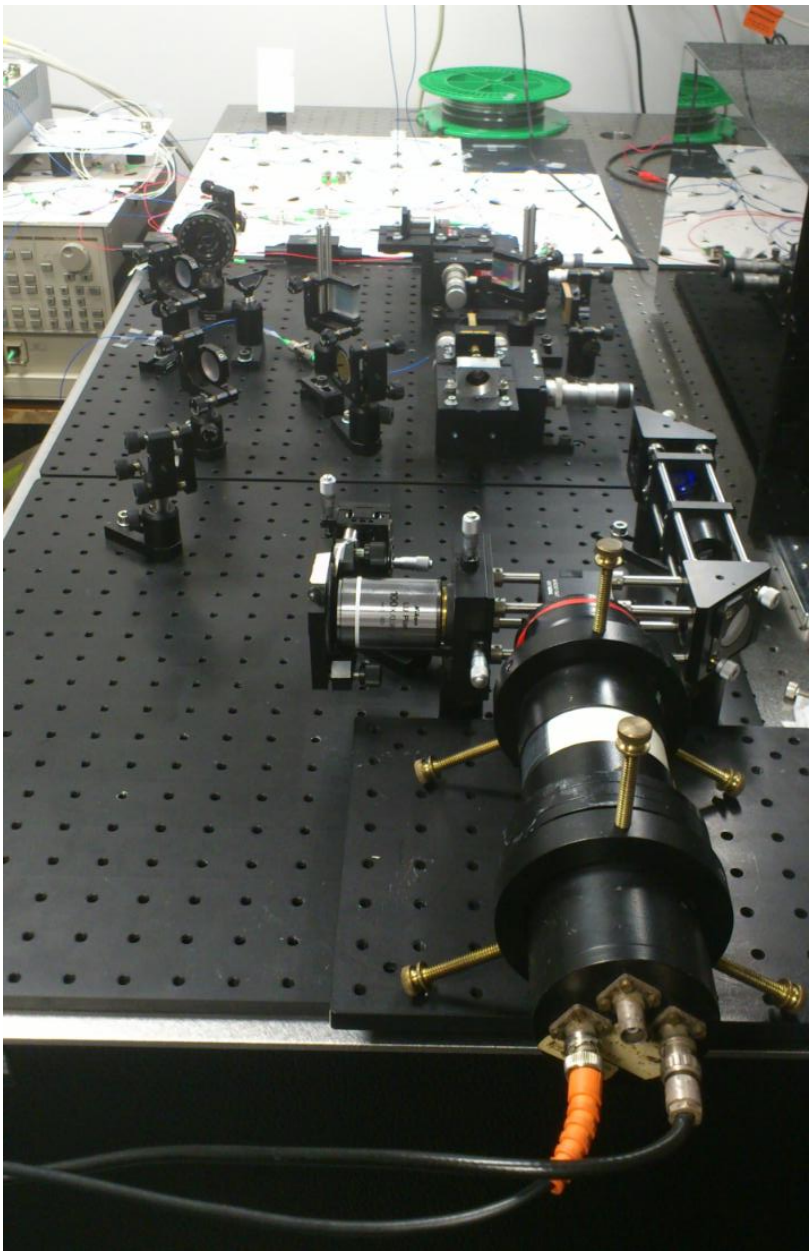

Microscope setup for imaging in the reflection mode.